

# SPECTROSCOPY AND HOT ELECTRON RELAXATION DYNAMICS IN SEMICONDUCTOR QUANTUM WELLS AND QUANTUM DOTS

---

Arthur J Nozik

*The National Renewable Energy Laboratory, Center for Basic Sciences,  
1617 Cole Boulevard, Golden, Colorado 80401, and Department of Chemistry,  
University of Colorado, Boulder, Colorado 80309; e-mail: anozik@nrel.nrel.gov*

**Key Words** hot-carrier cooling, high efficiency photovoltaics, semiconductor quantum dot arrays, superlattices, high efficiency photo electrochemistry

■ **Abstract** Photoexcitation of a semiconductor with photons above the semiconductor band gap creates electrons and holes that are out of equilibrium. The rates at which the photogenerated charge carriers return to equilibrium via thermalization through carrier scattering, cooling by phonon emission, and radiative and nonradiative recombination are important issues. The relaxation processes can be greatly affected by quantization effects that arise when the carriers are confined to regions of space that are small compared with their deBroglie wavelength or the Bohr radius of bulk excitons. The effects of size quantization in semiconductor quantum wells (carrier confinement in one dimension) and quantum dots (carrier confinement in three dimensions) on the respective carrier relaxation processes are reviewed, with emphasis on electron cooling dynamics. The implications of these effects for applications involving radiant energy conversion are also discussed.

## INTRODUCTION

Semiconductors have a fundamental threshold energy for the absorption of photons; this critical energy is termed the band gap ( $E_g$ ); photons with energies less than the band gap are not absorbed. The absorption of a photon creates an electron in the conduction band and leaves behind a positive charge, termed a hole, in the valence band. When the absorbed photon energy is greater than the band gap, the distribution of the excess energy between the electron and hole is given by

$$\Delta E_e = (h\nu - E_g) [1 + m_e^*/m_h^*]^{-1} \quad 1.$$

$$\Delta E_h = (h\nu - E_g) - \Delta E_e, \quad 2.$$

where  $m_e^*$  and  $m_h^*$  are the effective masses of electrons and holes, respectively,  $\Delta E_e$  is the energy difference between the conduction band and the initial energy of the

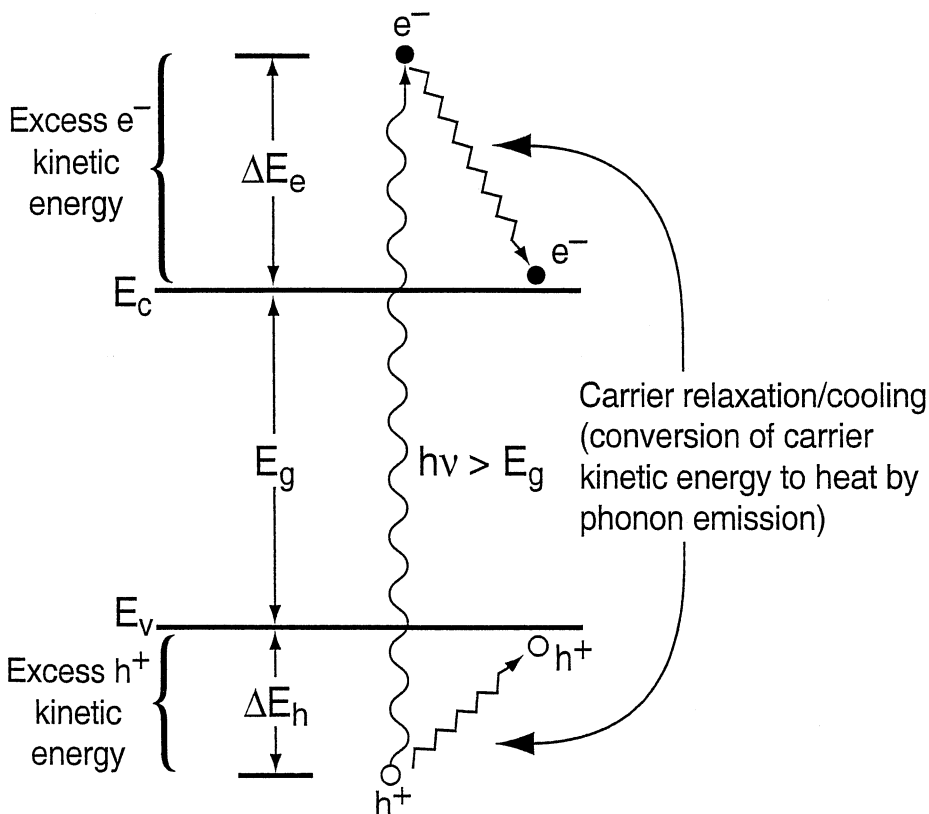


**Figure 1** Hot carrier relaxation/cooling dynamics in semiconductors.

photogenerated electron, and  $\Delta E_h$  is the energy difference between the valence band and the photogenerated hole (see Figure 1) (1, 2). These excess energies appear in the respective charge carriers (electrons and holes) as kinetic energy; such photogenerated carriers produced by the absorption of photons bigger than the bandgap are far from equilibrium. At thermal equilibrium the carriers would have a Boltzmann distribution determined by the temperature of the system, with electrons being within  $kT$  of the bottom of the conduction band and holes being within  $kT$  of the top of the valence band.

The photogenerated carriers can be produced by either a light pulse or steady-state illumination. In the former case, the carriers seek and establish equilibrium over a time period that depends upon the specific rates of the various equilibration pathways. In the latter case, with continuous optical pumping, a steady-state condition is reached in which a steady-state population of excited, nonequilibrated carriers is produced; the characteristics of this steady-state population will also depend upon the balance between the kinetics of the various equilibration pathways and the rate and energetics of carrier generation. In the

discussion immediately below we consider pulsed excitation for reasons of simplicity.

Pulsed excitation with a single wavelength produces initial carrier populations of electrons and holes that are nearly mono-energetic; they may not be perfectly mono-energetic because of possible multiplicities of hole states that are available for the optical transition. This possibility is strongest for semiconductors exhibiting quantum confinement (3). In either case, the initial carrier distributions are not Boltzmann-like, and the first step toward establishing equilibrium is for the electrons and holes to interact separately among themselves through their respective carrier-carrier collisions and intervalley scattering to form separate Boltzmann distributions of electrons and holes. The two Boltzmann distributions of electrons and holes can then be separately assigned an electron and hole temperature that reflects the distributions of kinetic energy in the respective charge carrier populations. If photon absorption produces electrons and holes, each with initial excess kinetic energies at least  $kT$  above the conduction and valence bands, then both initial carrier temperatures are always above the lattice temperature; these carriers are called hot carriers (i.e. hot electrons and hot holes). This first stage of relaxation or equilibration occurs very rapidly ( $<100$  fs) (4, 5), and this process is often referred to as carrier thermalization (i.e. formation of a thermal distribution described by Boltzmann statistics).

After the separate electron and hole populations come to equilibrium among themselves in less than 100 fs, they are still not yet in equilibrium with the lattice. The next step of equilibration is for the hot electrons and hot holes to equilibrate with the semiconductor lattice. The lattice temperature of the semiconductor is determined by equilibration of its quantized lattice vibrations (phonons) with the surroundings. The lattice temperature is the ambient temperature and is lower than the initial hot-electron and hot-hole temperatures. Equilibration of the hot carriers with the lattice is achieved through carrier-phonon interactions (phonon emission through electron- and hole-scattering) whereby the excess kinetic energy of the carriers is transferred from the carriers to the phonons; the phonons involved in this process are the longitudinal optical (LO) phonons. This may occur by each carrier undergoing separate interactions with the phonons or in an Auger process in which the excess energy of one carrier type is transferred to the other type, which then undergoes the phonon interaction. The phonon emission results in cooling of the carriers and heating of the lattice until the carrier and lattice temperatures become equal. This process is termed carrier cooling, but some researchers also refer to it as thermalization; however, this latter terminology can cause confusion with the first stage of equilibration that just establishes the Boltzmann distribution among the carriers. Here, we restrict the term thermalization to the first stage of carrier relaxation and we refer to the second stage as carrier cooling (or carrier relaxation) through carrier-phonon interactions.

The final stage of equilibration results in complete relaxation of the system. The electrons and holes can recombine, either radiatively or nonradiatively, to produce the final electron and hole populations that existed in equilibrium in the dark before photoexcitation. Another important possible pathway following

photoexcitation of semiconductors is for the photogenerated electrons and holes to undergo spatial separation. Separated photogenerated carriers can subsequently produce a photovoltage and a photocurrent (photovoltaic effect) (1, 2, 6); alternatively, the separated carriers can drive electrochemical oxidation and reduction reactions (generally labeled redox reactions) at the semiconductor surface (photoelectrochemical energy conversion) (7). These two processes form the basis for devices/cells that convert radiant energy (solar energy) into electrical (1, 2, 6) or chemical free energy (photovoltaic cells and photoelectrochemical cells, respectively) (7).

The dynamics of carrier cooling in semiconductors is an extremely important factor for many practical device applications. For example, high-efficiency negative electron affinity photocathodes depend upon hot-electron injection from p-type semiconductors into a vacuum (1). Hot-electron transistors depend upon hot-electron transport (2). For the application of quantum dots in novel quantum dot lasers, it is critical that hot photogenerated carriers relax before photon emission (8). For applications involving photon (radiant) energy conversion, the ultimate thermodynamic limit on conversion efficiency can be increased from about 32% for carriers fully equilibrated with the lattice in a single threshold (single band gap) semiconductor photoconverter, to about 66% for conversion utilizing hot carriers that have not undergone any interaction with phonons and are thus converted at their initial carrier temperatures (9, 10).

There are two fundamental ways to utilize hot carriers for enhancing the efficiency of photon conversion. One way produces an enhanced photovoltage, and the other way produces an enhanced photocurrent. The former requires that the carriers be extracted from the photoconverter before they cool (9, 10), whereas the latter requires the energetic hot carriers to produce a second (or more) electron-hole pair through impact ionization (11, 12). This latter process is the inverse of an Auger process whereby two electron-hole pairs recombine to produce a single highly energetic electron-hole pair. In order to achieve the former, the rates of photogenerated carrier separation, transport, and interfacial transfer across the semiconductor-molecule interface must all be fast compared with the rate of carrier cooling (10, 13–15). The latter requires that the rate of impact ionization (i.e. inverse Auger effect) is greater than the rate of carrier cooling. These processes and their potential applications in novel quantum dot solar cells are discussed later in “Quantum Dot Solar Cells.”

Hot electrons and hot holes generally cool at different rates because they generally have different effective masses; for most inorganic semiconductors electrons have effective masses that are significantly lighter than holes and consequently cool more slowly. Another important factor is that hot-carrier cooling rates are dependent upon the density of the photogenerated hot carriers (i.e. the absorbed light intensity) (4, 5, 16); this effect is discussed in “Hot-Electron Cooling Dynamics in Quantum Wells and Superlattices.” Here, most of the dynamical effects we discuss are dominated by electrons rather than holes; therefore, we restrict our subsequent discussion primarily to the relaxation dynamics of photogenerated electrons.

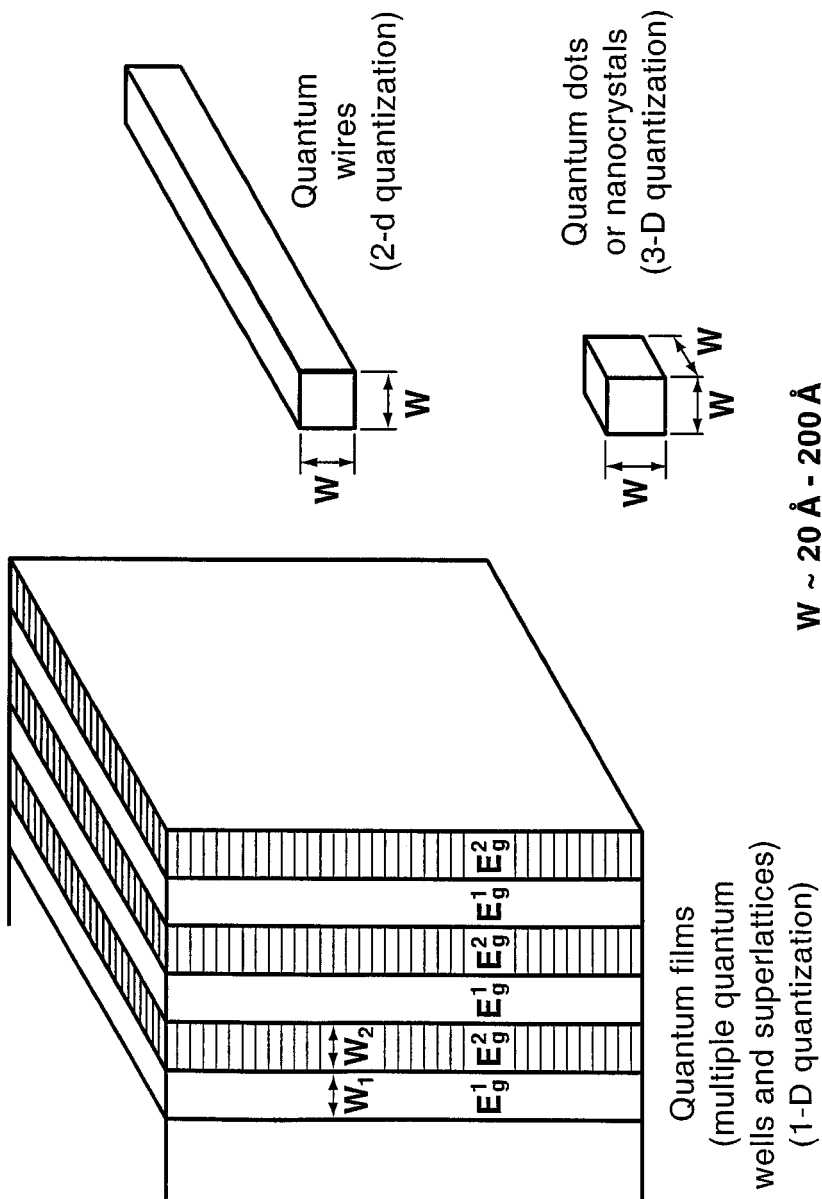
Finally, in recent years it has been proposed (10, 13, 14, 17–20), and experimentally verified in some cases (see “Hot-Electron Cooling Dynamics in Quantum Wells and Superlattices” and “Experimental Determination of Relaxation/Cooling Dynamics and a Phonon Bottleneck in Quantum Dots”), that the relaxation dynamics of photogenerated carriers may be markedly affected by quantization effects in the semiconductor (i.e. in semiconductor quantum wells, quantum wires, quantum dots, superlattices, and nanostructures). That is, when the carriers in the semiconductor are confined by potential barriers to regions of space that are smaller than or comparable to their deBroglie wavelength or to the Bohr radius of excitons in the semiconductor bulk, the relaxation dynamics can be dramatically altered; specifically, the hot-carrier cooling rates may be dramatically reduced, and the rate of impact ionization could be enhanced and become competitive with the rate of carrier cooling (21). These effects are discussed extensively in this review.

## RELAXATION DYNAMICS OF HOT ELECTRONS IN QUANTUM WELLS AND SUPERLATTICES

Semiconductors show dramatic quantization effects when charge carriers are confined by potential barriers to small regions of space where the dimensions of the confinement are less than their deBroglie wavelength; the length scale at which these effects begin to occur ranges from about 10 to 50 nm for typical semiconductors (groups IV, III-V, II-VI). In general, charge carriers in semiconductors can be confined by potential barriers in one, two, or three spatial dimensions. These regimes are termed quantum films, quantum wires, and quantum dots, respectively (see Figure 2). Quantum films are also more commonly referred to simply as quantum wells (QWs). This is because quantum films were the first quantized semiconductor nanostructures to be studied extensively beginning in the 1970s (22). These structures were produced by molecular beam epitaxy (MBE) and metallo-organic chemical vapor deposition (MOCVD) and represented textbook examples of a one-dimensional quantum well (23–27).

One-dimensional quantum wells, hereafter called quantum films or just quantum wells, are usually formed through epitaxial growth of alternating layers of semiconductor materials with different band gaps. A single QW is formed from one semiconductor sandwiched between two layers of a second semiconductor having a larger band gap; the center layer with the smaller band gap forms the QW while the two layers sandwiching the center layer create the potential barriers (28) (see Figure 6.6 of Reference 28). Two potential wells are actually formed in the QW structure; one is for conduction band electrons, the other for valence-band holes. The well depth for electrons is the difference (i.e. the offset) between the conduction band edges of the well and barrier semiconductors, whereas the well depth for holes is the corresponding valence band offset (see Figure 6.6 of Reference 28). If the offset for either the conduction or valence bands is zero, then only one carrier will be confined in a well.

## Quantization Configurations



Multiple quantum well structures consist of a series of QWs (i.e. a series of alternating layers of wells and barriers). If the barrier thickness between adjacent wells prevents significant electronic coupling between the wells, then each well is electronically isolated; this type of structure is termed a multiple quantum well (MQW). Alternatively, if the barrier thickness is sufficiently thin to allow electronic coupling between wells (i.e. there is significant overlap of the electronic wavefunctions between wells), then the electronic charge distribution can become delocalized along the direction normal to the well layers. This coupling also leads to a broadening of the quantized electronic states of the wells; the new broadened and delocalized quantized states are termed minibands (see Figure 3). A multiple QW structure that exhibits strong electronic coupling between the wells is termed a superlattice. The critical thickness at which miniband formation just begins to occur is about 40 Å (27, 29); the electronic coupling increases rapidly with decreasing thickness, and miniband formation is very strong below 20 Å (27) (see Figure 18, Chapter 1 of Reference 27). Superlattice structures yield efficient charge transport normal to the layers because the charge carriers can move through the minibands; the narrower the barrier, the wider the miniband and the higher the carrier mobility. Normal transport in MQW structures (thick barriers) requires thermionic emission of carriers over the barriers or, if electric fields are applied, field-assisted tunneling through the barriers (30).

## Energy Levels and Density of States in Quantum Wells and Superlattices

The confinement of electrons or holes in potential wells leads to the creation of discrete energy levels in the wells, compared to the continuum of states in bulk material; quantization also leads to a major change in the density of states. The energy levels can be calculated by solving the Schrödinger equation for the well-known “particle in a box” problem. Using the effective mass envelope function approximation (27, 31–34), the electron wave function,  $\Psi_n$ , is

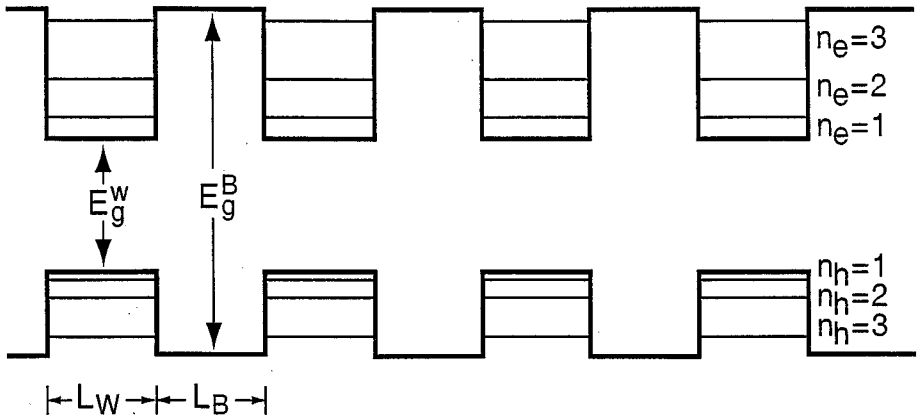
$$\Psi_n = \sum_{W,B} e^{i\mathbf{k}\cdot\mathbf{r}} U_{\mathbf{k}}^{W,B}(\mathbf{r}) \phi_n(z), \quad 3.$$

where  $W$  and  $B$  refer to well and barrier, respectively;  $k$  is the transverse electron wave vector;  $z$  is the growth direction,  $U_{\mathbf{k}}^{W,B}(\mathbf{r})$  is the Bloch wave function in  $W$  or  $B$ ; and  $\phi_n(z)$  is the envelope wave function. The envelope wave function is determined by solving the Schrödinger equation:

$$\left( \frac{\hbar^2}{2m^*} \frac{\partial^2}{\partial z^2} + V_c(z) \right) \phi_n(z) = E_n \phi_n(z), \quad 4.$$

**Figure 2** Three types of quantization configurations. The type depends upon the dimensionality of carrier confinement.

### Multiple Quantum Wells



### Superlattice

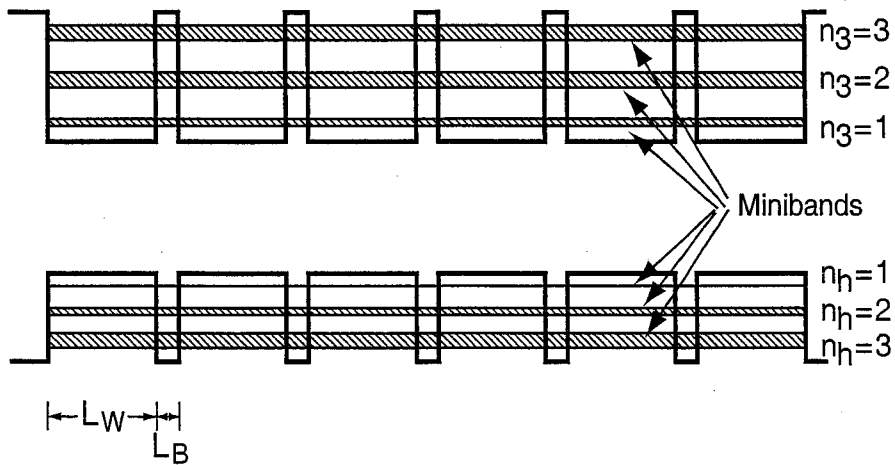


**Figure 3** Difference in electronic states between multiple quantum well structures (barriers  $>40 \text{ \AA}$ ) and superlattices (barriers  $<40 \text{ \AA}$ ); miniband formation occurs in the superlattice structure, which permits carrier delocalization.

where  $V_c(z)$  is the potential barrier function, and  $E_n$  is the quantized energy level in the well.

Considering first isolated QWs that are infinitely deep, the solution to Equation 4 becomes very simple because the wave functions must be zero at the well-barrier interfaces. This leads to the well-known solutions:

$$\psi_n = A \sin \frac{n\pi z}{L_w} \quad 5.$$

$$E_n = \frac{\hbar^2}{2m^*} \left( \frac{n\pi}{L_w} \right)^2, \quad n = 1, 2, 3, \dots, \quad 6.$$

where  $L_w$  is the well width.

For the more realistic case of finite barrier heights, where the effective masses in the well and barrier are taken to be equal,

$$\phi_n(z) = A \cos kz \quad (\text{inside well}) \quad 7.$$

$$= B \exp[-k(z - L_w/2)] \quad (\text{outside well}), \quad 8.$$

where

$$E_n = \frac{\hbar^2 k^2}{2m^*} - V_o \quad -V_o < E_n < 0 \quad 9.$$

and

$$\cos(kL_w/2) = k/k_o \quad \text{for} \quad \tan kL_w/2 > 0 \quad 10.$$

$$\sin(kL_w/2) = k/k_o \quad \text{for} \quad \tan kL_w/2 > 0, \quad 11.$$

where

$$k_o = 2m^*V_o/\hbar^2, \quad \text{and} \quad V_o \text{ is the barrier height.} \quad 12.$$

There is always at least one state in the well no matter how thin it is; the number of bound states is given by:

$$1 + \text{Int} \left[ \frac{(2m^*V_oL_w^2)^{1/2}}{\pi^2\hbar^2} \right], \quad 13.$$

where  $\text{Int}(x)$  indicates the integer part of the argument.

The calculation of the hole levels is much more complicated because the band structure of many important semiconductors has hole bands with fourfold degeneracy at  $k = 0$ . This leads to heavy and light holes with different effective masses. Consequently, in the QW a double set of hole energy levels is formed with different spacings between levels—one set for the light holes, the second set for the heavy holes (see Figure 6.6 of Reference 28). Solutions to the problem have been reported for both infinite (31, 33) and finite (34) potential barriers.

For superlattices several approaches have been used to calculate the energy level structure of the minibands (31, 33, 34). One approach is to use a tight-binding model for the multiple wells leading to a Bloch-like envelope function of the form (27, 35).

$$\psi_q^i(z) = \frac{1}{\sqrt{N_w}} \sum_l e^{iqlx} \phi^i(z - lx), \quad 14.$$

where  $N_w$  is the number of wells,  $\phi(z - lx)$  is the  $i$ th wave function of the QW centered at  $z = lx$  and  $q$  is the Bloch wave vector.

This approach leads to results that are summarized in Figure 18, Chapter 1 of Reference 27, which shows the energy levels as a function of barrier thickness. That figure shows the formation of minibands with energy band widths that increase rapidly with decreasing barrier widths below 40 Å.

The density of states (DOS or  $N(E)$ ) also shows profound changes with the dimensionality of quantization. For ideal bulk semiconductors with simple parabolic energy bands, the DOS has a square root dependence on electron energy

$$N(E)_{Bulk} = \sqrt{2}(m^*)^{3/2} \pi^{-2} \hbar^{-3} E^{1/2}. \quad 15.$$

For an ideal QW the DOS shows a step-like function with each plateau having a DOS of:

$$N(E)_{QW} = nm^* / \pi \hbar^2, \quad 16.$$

where  $n$  is the quantum number of the state.

For a superlattice the steepness of the steps is destroyed by the dispersion of the  $N$  states in a miniband (23, 27):

$$N(E)_{SL} = N \frac{m^*}{\pi \hbar^2} \arccos \left( \frac{\varepsilon_i - E_i - s_i}{2t_i} \right) \quad 17.$$

where  $\varepsilon_i$ ,  $s_i$ , and  $t_i$  are defined by Equations 29 and 30, Chapter 1 of Reference 27. These DOS functions for bulk semiconductors, QWs, superlattices, quantum wires, and quantum dots are shown in Figure 6.2 of Reference 28 and in Figure 17, Chapter 1 of Reference 27; the DOS for quantum dots exhibits discrete values at the discrete quantized energy levels.

## Fabrication of Quantum Wells and Superlattices

QWs are produced through epitaxial growth of crystalline films via either molecular beam epitaxy (MBE) or metallo-organic chemical vapor deposition (MOCVD). Both of these techniques are capable of creating epitaxial layers of sufficient quality to produce quantization effects. These qualities include film thickness uniformity and interfacial abruptness (both within a few atomic layers), crystalline perfection, and compositional uniformity.

**Molecular Beam Epitaxy** In this system an ultrahigh-vacuum chamber is outfitted with a number of evaporation (i.e. effusion) cells, each controlled by a separate shutter, which supply fluxes of molecular beams of the desired atomic species. The beams can be turned on and off within 0.1 sec. Growth rates are typically 5 Å/sec. An ion-beam sputtering gun is used first to ion etch the surfaces to remove impurities and imperfections. The substrate is maintained at about 500–700°C during growth. Various spectroscopic capabilities, such as mass spectrometry, Auger spectroscopy, and reflection high-energy electron diffraction, are included in the chamber to control the process and provide analytical data on the quality of the films. The atomic and molecular species that can be produced by MBE include Ga, Al, In, As, Sb, Sn, Be, Ge, Se, Te, Cd, Hg, Zn, Mn, Pb, and Si. The most common QW materials produced by MBE are the III-V semiconductor binary and ternary compounds, such as GaAs/Al<sub>x</sub>Ga<sub>1-x</sub>As, GaSb/Al<sub>x</sub>Ga<sub>1-x</sub>Sb, InAs/GaAs, Ga<sub>x</sub>In<sub>1-x</sub>As/Al<sub>x</sub>In<sub>1-x</sub>As, GaAs/Ga<sub>x</sub>In<sub>1-x</sub>P<sub>2</sub>, and InP/Ga<sub>x</sub>In<sub>1-x</sub>As. Some II-VI semiconductor QWs have also been prepared, such as CdTe/HgTe and ZnSe/Zn<sub>1-x</sub>Mn<sub>x</sub>Se.

**Metallo-Organic Chemical Vapor Deposition** The MOCVD process is generally only used to prepare III-V semiconductor QWs. In this process the group III metals are introduced into a reaction chamber in the form of metallo-organic vapors that react at high temperatures with gaseous precursors of the nonmetalloid group V component of the desired semiconductor compound to form a crystalline, epitaxial film on a heated substrate. Ga, Al, and In are commonly introduced as trimethyl gallium (TMG), trimethyl aluminum (TMA), and trimethyl indium (TMI). As and P are usually introduced as arsine and phosphine, although less toxic compounds such as tertiary butyl arsine and tertiary butyl phosphine are being increasingly utilized. The organometallic compounds are kept in liquid form at a sufficiently low, but constant, temperature and are swept into the reaction chamber at a controlled composition by sparging hydrogen gas at a controlled flow rate through the liquid metallo-organics. Gaseous arsine or phosphine is fed directly into the system from gas cylinders through flow and pressure controllers; ultrapure hydrogen is used as the carrier gas for all reactant flows. The single crystal substrate is placed on a graphite block that is heated either by radio frequency (RF) or resistance heaters to 650 to 750°C. Growth rates are typically 5–10 Å/sec.

The reaction chamber is operated either at atmospheric pressure or at reduced pressure (50–100 torr). The low pressure system can yield very sharp interfaces between the semiconductor heterojunctions and very uniform epilayers (see Figure 4).

## Optical Spectroscopy of Quantum Wells and Superlattices

**Optical Absorption** Optical transitions between quantum levels can occur upon excitation with light. The interband transition probability is the product of an optical matrix element (M) times a DOS. M involves the electric dipole operator

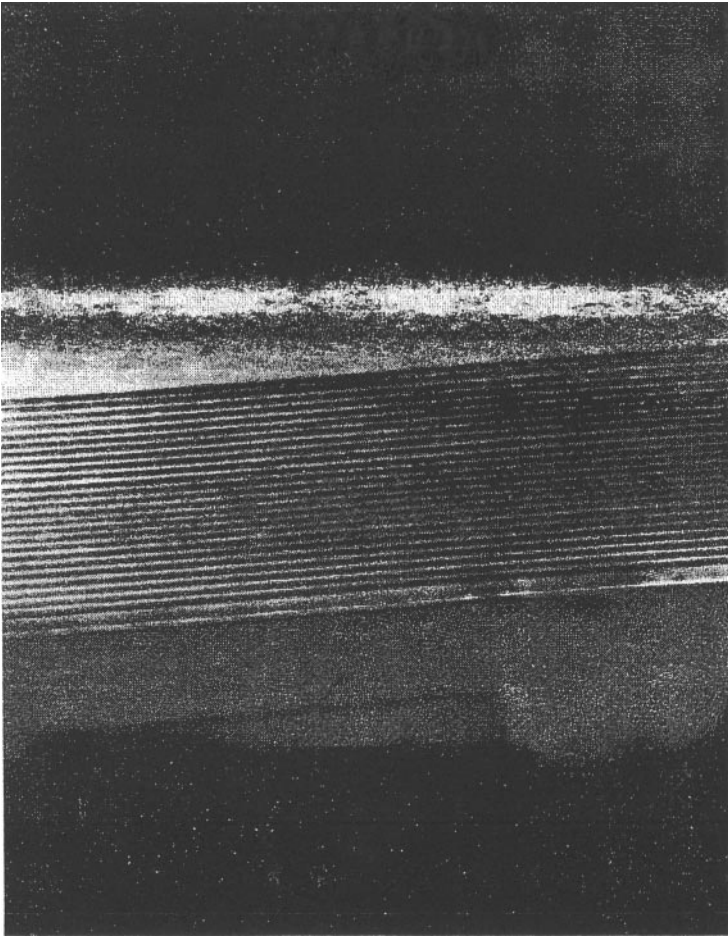


**Figure 4** TEM of GaAs/Al<sub>0.32</sub>Ga<sub>0.68</sub>As superlattice structure. GaAs wells are 52 Å thick, and the Al<sub>0.32</sub>Ga<sub>0.68</sub>As barriers are 17 Å thick.

and can be expressed as (23)

$$M = \langle \phi_e(z) e^{ik_e \cdot r} U_{cke}(r) | \eta | \phi_h(z) e^{ik_h \cdot r} U_{vkh}(r) \rangle, \quad 18.$$

where  $\phi_e(z)$  and  $\phi_h(z)$  are the electron and hole envelope wave functions,  $k_e$  and  $k_h$  are electron and hole wave vectors,  $\eta$  is the polarization vector of the light, and  $U_{cke}(r)$  and  $U_{vkh}(r)$  are the Bloch functions. The integration of Equation 18 produces a factor  $[\phi_e(z) \phi_h(z)]$ , which becomes unity for transitions between electron and hole states with the same quantum number. Thus, the selection rule for optical interband transitions is that  $\Delta n = 0$ , where  $n$  is the quantum number of the energy level in the well. Some additional factors affecting optical transitions are: (a) Heavy hole–electron transitions are expected to be three times stronger

than light hole–electron transitions; (b) transitions involving different  $n$  values become possible in the presence of an electric field and also when finite wells are considered; and (c) parity is a good quantum number, and transitions involving the same parity are allowed.

In light of the above discussion, the optical absorption spectrum of a quantum film is expected to consist of a series of steps, with the position of these steps corresponding to the transitions between heavy- or light hole–quantum states and electron quantum states following the selection rule  $\Delta n = 0$ . Furthermore, because the widths of the wells are commonly smaller than the calculated diameter of an exciton, the exciton binding energy is greatly increased in QWs, and the excitons can be stable even at room temperature. Thus, the absorption spectra of QWs can be expected to show exciton peaks, even at room temperature, which occur at energies below the step. Such spectra have indeed been observed by many workers (22, 35).

**Photoreflectance Spectroscopy** Photoreflectance (PR) is one of the powerful spectroscopic techniques for characterizing the electronic energy level structure of QWs. PR is particularly sensitive to the optical transitions in the well because the observed signal reflects the third derivative of the optical constants (36, 37). The experiment is performed by modulating the electric field in the space charge region of the sample with a pump beam having a photon energy above the band gap, and scanning the sample with an overlapping probe beam that is swept through the desired photon energy range. The pump beam is typically from a laser, whereas the probe beam is at low intensity and produced by passing white light from a lamp through a monochromator. The reflectivity of the probe beam is measured as a function of photon energy ( $E$ ), and the fractional change in reflectivity is given by

$$\Delta R/R = \text{Re} \left| \sum_j [C_j e^{i\theta_j} (E - E_{gj} + i\Gamma_j)^{-p_j}] \right|, \quad 19.$$

where subscript  $j$  refers to the  $j$ th transition,  $C$  is the amplitude,  $E_g$  is the transition energy,  $\Gamma$  is the broadening parameter,  $2$  is the phase, and  $p$  denotes the type of critical point for the transition and the order of its derivative (38). The value of  $p$  depends upon whether the transitions involve localized (e.g. excitonic) or delocalized states (e.g. minibands). The sample can be run in air or as an electrode in a photoelectrochemical cell; in the former case the space charge is produced through equilibration with intrinsic surface states.

PR spectroscopy is very sensitive (29), as illustrated in Figure 1 of Reference 29, in which the PR spectrum of a superlattice containing 20 periods of 250 Å GaAs wells and 17 Å  $\text{Al}_{0.28}\text{Ga}_{0.72}\text{As}$  barriers is shown; 32 optical transitions can be clearly seen in the spectrum (29). Because of the thin barriers in this superlattice sample, strong miniband formation occurs with appreciable miniband widths. The calculated energy levels for this sample showing the miniband structure is presented in Figure 6.13 of Reference 28. Transitions to the top and bottom of a

given miniband can be observed in PR spectroscopy; the predicted 32 transitions satisfying the selection rule  $\Delta n = 0$  are compared with the observed PR transitions in Figure 6.12c of Reference 28. The agreement is excellent. It is quite impressive that PR can resolve the transitions between minibands even when the minibands overlap each other in energy.

## Hot Electron Cooling Dynamics in Quantum Wells and Superlattices

Hot-electron cooling times can be determined from several types of time-resolved photoluminescence (PL) experiments. One technique involves hot luminescence nonlinear correlation (39–41), which is a symmetrized pump-probe type of experiment. Figure 2 of Reference 39 compares the hot-electron relaxation times as a function of the electron energy level in the well for bulk GaAs and a 20-period MQW of GaAs/Al<sub>0.38</sub>Ga<sub>0.62</sub>As containing 250 Å GaAs wells and 250 Å Al<sub>0.38</sub>Ga<sub>0.62</sub>As barriers. For bulk GaAs the hot-electron relaxation time varies from about 5 ps near the top of the well to 35 ps near the bottom of the well. For the MQW the corresponding hot-electron relaxation times are 40 ps and 350 ps.

Another method uses time-correlated single photon counting to measure PL lifetimes of hot electrons. Figure 5 shows 3-dimensional (3-D) plots of PL intensity as a function of energy and time for bulk GaAs and a 250 Å GaAs/250 Å Al<sub>0.38</sub>Ga<sub>0.62</sub>As MQW (16). It is clear from these plots that the MQW sample exhibits much longer-lived hot luminescence (i.e. luminescence above the lowest  $n = 1$  electron to heavy-hole transition at 1.565 eV) than bulk GaAs. Depending upon the emitted photon energy, the hot PL for the MQW is seen to exist beyond times ranging from hundreds to several thousand ps. On the other hand, the hot PL intensity above the band gap (1.514 eV) for bulk GaAs is negligible over most of the plot; it is only seen at the very earliest times and at relatively low photon energies.

Calculations were performed (16) on the PL intensity versus time and energy results to determine the time dependence of the quasi-Fermi-level, electron temperature, electronic specific heat, and ultimately the dependence of the characteristic hot-electron cooling time on electron temperature.

The cooling, or energy-loss, rate for hot electrons is determined by longitudinal optical (LO) phonon emission through electron-LO-phonon interactions. The time constant characterizing this process can be described by the following expression (42–44):

$$P_e = -\frac{dE}{dt} = \frac{\hbar\omega_{LO}}{\tau_{avg}} \exp(-\hbar\omega_{LO}/kT_e), \quad 20.$$

where  $P_e$  is the power loss of electrons (i.e. the energy-loss rate),  $\hbar\omega_{LO}$  is the LO phonon energy (36 meV in GaAs),  $T_e$  is the electron temperature, and  $\tau_{avg}$  is the time constant characterizing the energy-loss rate.

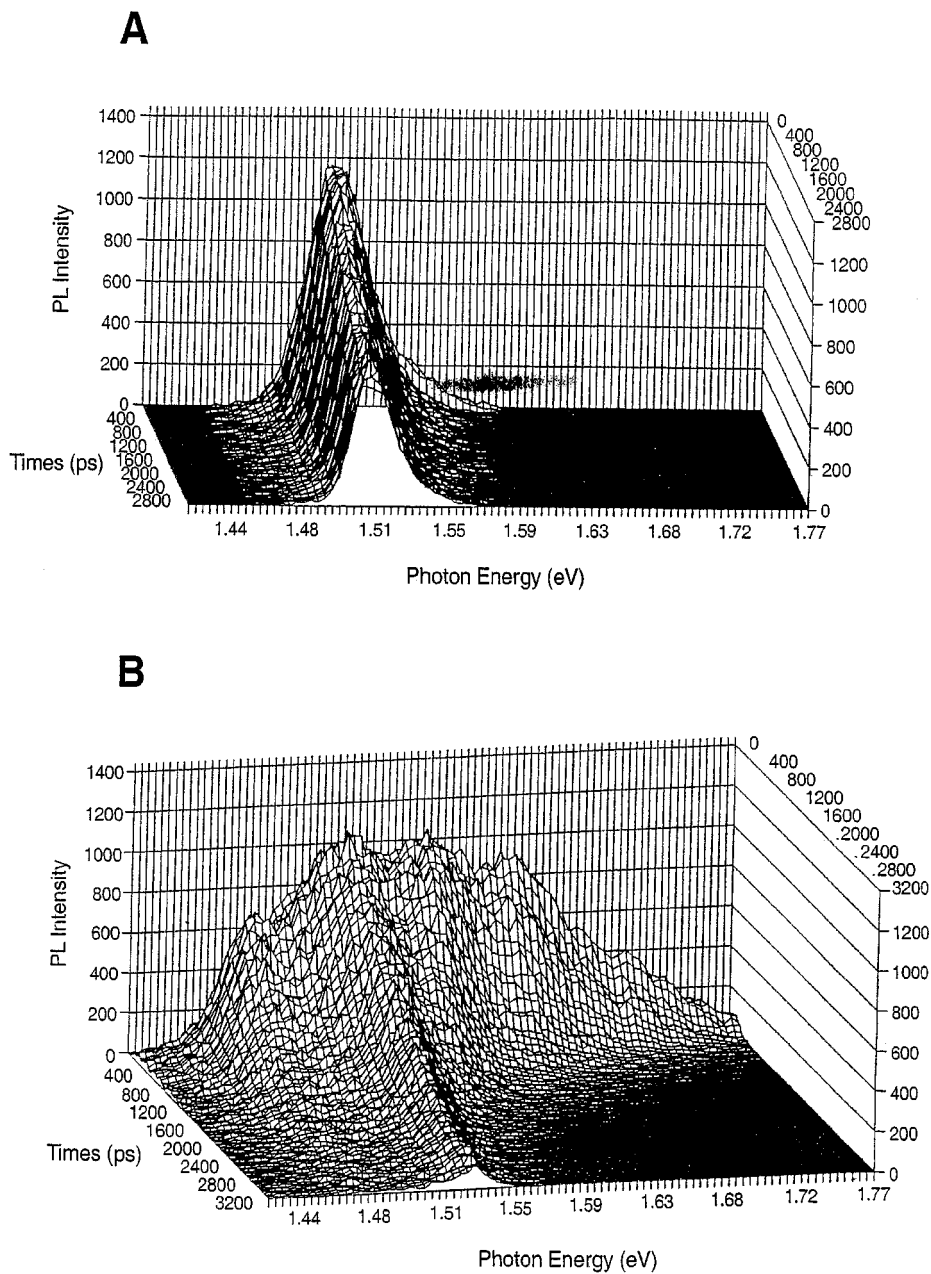


**Figure 5** Three-dimensional plots of photoluminescence intensity versus time and photon energy for (A) bulk GaAs and (B) 250 Å GaAs/250 Å Al<sub>0.38</sub>Ga<sub>0.62</sub>As MQW (16).

The electron energy–loss rate is related to the electron temperature–decay rate through the electronic specific heat. Because at high light intensity the electron distribution becomes degenerate, the classical specific heat is no longer valid. Hence, the temperature- and density-dependent specific heat for both the QW and bulk samples need to be calculated as a function of time in each experiment so that  $\tau_{avg}$  can be determined.

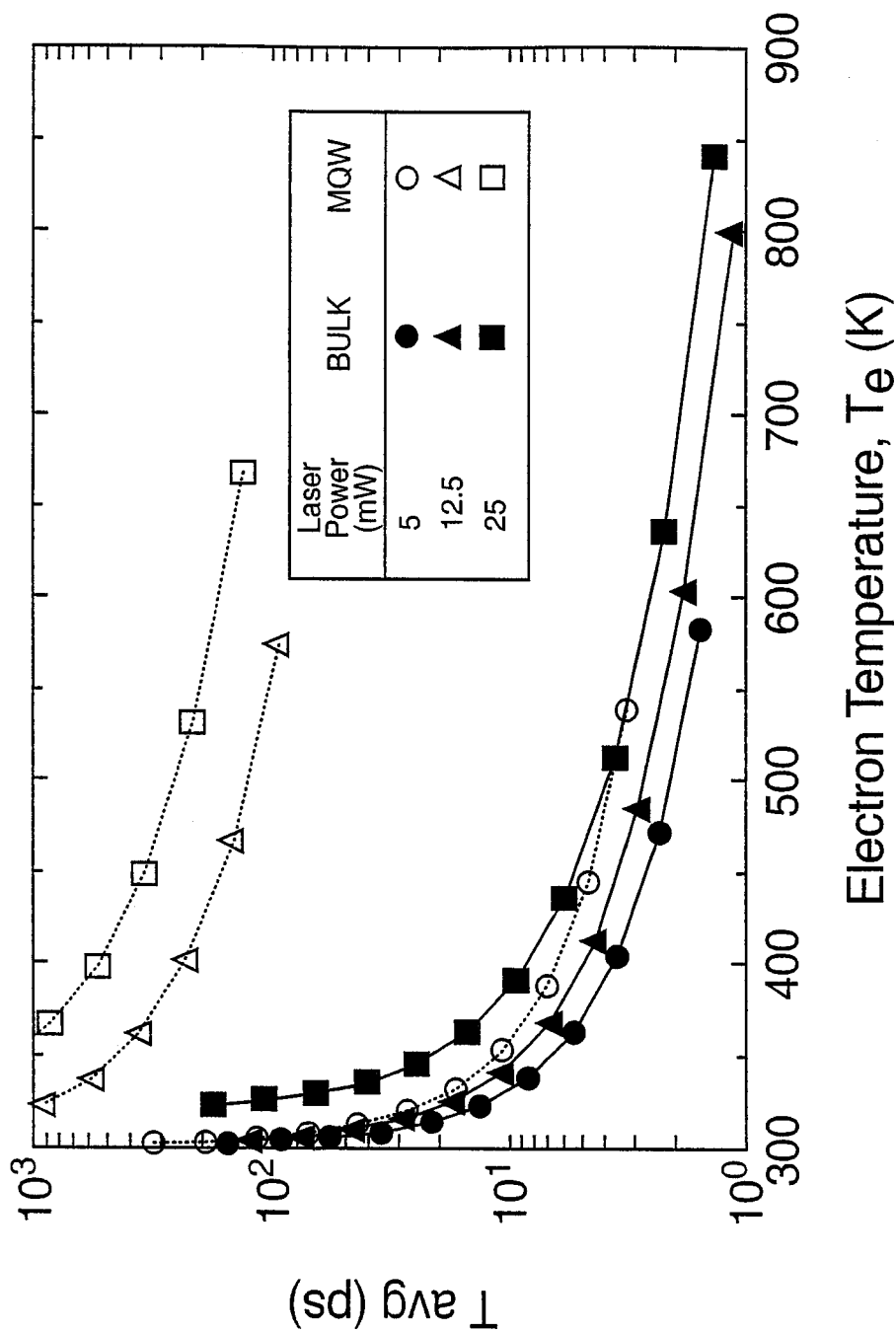
The results of such calculations (presented in Figure 2 of Reference 16) show a plot of  $\tau_{avg}$  versus electron temperature for bulk and MQW GaAs at high and low carrier densities. These results show that at a high carrier density [ $n_c \sim (2 - 4) \times 10^{18} \text{ cm}^{-3}$ ] the  $\tau_{avg}$  values for the MQW are much higher ( $\tau_{avg} = 350\text{--}550 \text{ ps}$  for  $T_e$  between 440 and 400 K) compared to bulk GaAs ( $\tau_{avg} = 10\text{--}15 \text{ ps}$  over the same  $T_e$  interval). Alternatively, at a low carrier density [ $n_c \sim (3\text{--}5) \times 10^{17} \text{ cm}^{-3}$ ] the differences between the  $\tau_{avg}$  values for bulk and MQW GaAs are much smaller.

A third technique used to measure cooling dynamics is PL upconversion (16). Time-resolved luminescence spectra were recorded at room temperature for a 4000-Å bulk GaAs sample at the incident pump powers of 25, 12.5, and 5 mW. The electron temperatures were determined by fitting the high-energy tails of the spectra; only the region that is linear on a semilogarithmic plot was chosen for the fit. The carrier densities for the sample were  $1 \times 10^{19}$ ,  $5 \times 10^{18}$ , and  $2 \times 10^{18} \text{ cm}^{-3}$ , corresponding to the incident excitation powers of 25, 12.5, and 5 mW, respectively. Similarly, spectra for the MQW sample were recorded at the same pump powers as the bulk. Figure 6 shows  $\tau_{avg}$  for bulk and MQW GaAs at the three light intensities, again showing the much slower cooling in MQWs (by up to two orders of magnitude).

The difference in hot-electron relaxation rates between bulk and quantized GaAs structures is also reflected in time-integrated PL spectra. Typical results are shown in Figure 7 for single photon counting data taken with 13 ps pulses of 600 nm light at 800 kHz focused to about  $100 \mu\text{m}$  with an average power of 25 mW (45). The time-averaged electron temperatures obtained from fitting the tails of these PL spectra to the Boltzmann function show that the electron temperature varies from 860 K for the 250 Å/250-Å MQW to 650 K for the 250 Å/17-Å superlattice, whereas bulk GaAs has an electron temperature of 94 K, which is close to the lattice temperature (77 K). The variation in the electron temperatures between the quantized structures can be attributed to differences in electron delocalization between MQWs and superlattices (SLs), and the associated nonradiative quenching of hot-electron emission.

As shown above, the hot-carrier cooling rates depend upon photogenerated carrier density; the higher the electron density, the slower the cooling rate. This effect is also found for bulk GaAs, but it is much weaker compared with quantized

**Figure 6** Time constant for hot-electron cooling ( $\tau_{avg}$ ) versus electron temperature for bulk GaAs and GaAs multiple quantum wells at three excitation intensities (16).



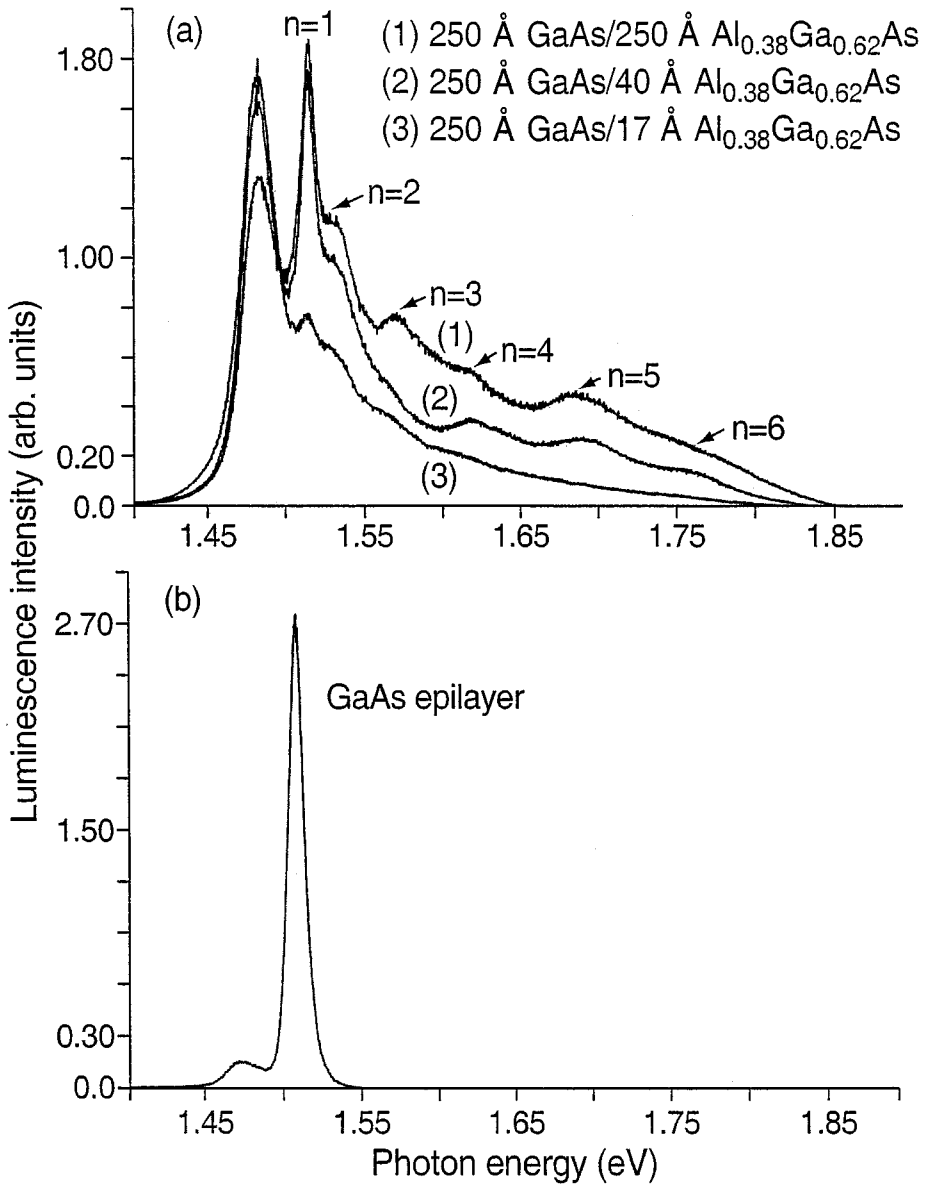


**Figure 7** (a) Time-integrated photoluminescence spectra for multiple quantum wells and SLs showing hot luminescence tails and high energy peaks arising from hot-electron radiative recombination from upper quantum levels. (b) Equivalent spectrum for bulk GaAs showing no hot luminescence (45).

GaAs. The most generally accepted mechanism for the decreased cooling rates in GaAs QWs is an enhanced “hot-phonon bottleneck” (46–48). In this mechanism a large population of hot carriers produces a nonequilibrium distribution of phonons (in particular, LO phonons that are the type involved in the electron-phonon interactions at high carrier energies) because the LO phonons cannot equilibrate fast enough with the crystal bath; these hot LO phonons can be reabsorbed by the electron plasma to keep it hot. In QWs the phonons are confined in the well and they exhibit slab modes (47), which enhance the hot-phonon bottleneck effect.

## RELAXATION DYNAMICS OF HOT ELECTRONS IN QUANTUM DOTS

As discussed above in “Hot-Electron Cooling Dynamics in Quantum Wells and Superlattices,” slowed hot-electron cooling in QWs and superlattices that is produced by a hot phonon bottleneck requires very high light intensities to create the required photogenerated carrier density of greater than about  $1 \times 10^{18} \text{ cm}^{-3}$ . This required intensity, possible with laser excitation, is many orders of magnitude greater than that provided by solar radiation at the Earth’s surface (maximum solar photon flux is about  $10^{18} \text{ cm}^{-2} \text{ s}^{-1}$ ; assuming a carrier lifetime of 1 ns and an absorption coefficient of  $1 \times 10^5 \text{ cm}^{-1}$ , this translates into a photoinduced electron density of about  $10^{14} \text{ cm}^{-3}$  at steady state). Hence, it is not possible to obtain slowed hot-carrier cooling in semiconductor QWs and superlattices with solar irradiation via a hot-phonon bottleneck effect; solar concentration ratios greater than  $10^4$  would be required, resulting in severe practical problems.

However, the situation with 3-D confinement in quantum dots (QDs) is potentially more favorable. In the quantum dot case, slowed hot-electron cooling is theoretically possible even at arbitrarily low light intensity; this effect is simply called a phonon bottleneck, without the qualification of requiring hot phonons (i.e. a nonequilibrium distribution of phonons). Furthermore, there is a possibility that the slowed cooling could make the rate of impact ionization (inverse Auger effect) an important process in QDs (21). PL blinking in QDs (intermittent PL as a function of time) has been explained (49, 50) by an Auger process whereby if two electron-holes pairs are photogenerated in a QD, one pair recombines and transfers its recombination energy to one of the remaining charge carriers, ionizing it over the potential barrier at the surface into the surface region. This creates an electric dipole in the QD that quenches subsequent radiative emission after subsequent photon absorption; after some time the ionized electron can return to the QD core, and the PL is turned on again. Because this Auger process can occur in QDs, the inverse Auger process, whereby one high energy electron-hole pair (created from a photon with  $h\nu > E_g$ ) can generate two electron-hole pairs, can also occur in QDs (21). The following discussion first presents general properties of quantum dots followed by a discussion of the hot-carrier cooling dynamics.

## Energy Levels and Density of States in Quantum Dots

The earliest and simplest treatment of the electronic states of a QD is based on the effective mass approximation (EMA); the simple EMA treatment was subsequently improved by incorporating the  $\mathbf{k} \bullet \mathbf{p}$  approach that has been commonly used to calculate the electronic structure of bulk semiconductor and QW structures.

The EMA rests on the assumption that if the QD is larger than the lattice constants of the crystal structure, then it will retain the lattice properties of the infinite crystal and the same values of the carrier effective masses; the electronic properties of the QD can then be determined by simply considering the modification of the energy of the charge carriers produced by the quantum confinement. Thus, the electronic properties are determined by solving the Schrödinger equation for a particle in a 3-D box. The zero<sup>th</sup> order approximation is a perfectly spherical QD with infinite potential walls at the surface. Strong confinement is defined as the case where the QD size is small compared with the deBroglie wavelength of electrons in the box or compared with the Bohr radius of the electrons; this is the case for II-VI and III-V semiconductors. Taking into account the Coulomb interaction between electrons and holes that is enhanced owing to confinement in the QD, the Hamiltonian can then be written as

$$\hat{H} = -\frac{\hbar^2 \nabla_e^2}{2m_e^*} - \frac{\hbar^2 \nabla_h^2}{2m_h^*} - \frac{e^2}{\varepsilon|r_e - r_h|} + V_e(r_e) + V_h(r_h) \quad 21.$$

and

$$\hat{H}\Psi(r) = E\Psi(r), \quad 22.$$

where  $V_e$  and  $V_h$  are the confining potentials,  $r_e$  and  $r_h$  are the distances of the electron and hole from the center of the QD, and  $\varepsilon$  is the dielectric constant of the semiconductor.

Analytical solutions of Equations 21 and 22 are difficult because center-of-mass motion and reduced mass motion cannot be separated as independent coordinates. Various approaches to solving this problem have been used. These include perturbation theory (51, 52), variational calculations (53–59), matrix diagonalization (60, 61), and Monte Carlo methods (62). Perturbation theory (51, 52) and variational calculations (57) lead to a solution of the form

$$E_{\min} = \frac{\hbar^2 \pi^2}{2R^2} \left[ \frac{1}{m_e^*} + \frac{1}{m_h^*} \right] - \frac{1.8e^2}{\varepsilon R} - 0.25E_{Ryd}^*, \quad 23.$$

where  $E_{\min}$  is the lowest energy separation between hole and electron states in the QD,  $E_{Ryd}^*$  is the bulk exciton binding energy in meV, and  $R$  is the QD radius.  $E_{\min}$  is often referred to as the band gap of the QD because it represents the threshold energy for photon absorption, blue-shifted from the bulk band gap,  $E_g$ .

Improvements in the EMA model involve accounting for band nonparabolicity and hole-state mixing (63–68), finite barrier heights (56), and surface polarization (69).

In the effective mass  $\mathbf{k} \cdot \mathbf{p}$  approach, the QD wavefunctions are expanded as a linear combination of  $N_b$  bulk Bloch functions at the  $\mathbf{k} = 0$  Brillouin zone center ( $\Gamma$  point) (64, 67); for these calculations values of  $N_b$  up to 8 (termed the 8-band  $\mathbf{k} \cdot \mathbf{p}$  model) have been used (70). The effective mass  $\mathbf{k} \cdot \mathbf{p}$  approach has been used very extensively for QDs, but recently its validity has been attacked (71–73) and vigorously defended (74, 75). An alternative approach based on direct diagonalization and pseudopotentials has been proposed as a better theoretical approach to calculate the electronic states in QDs (71, 72); the debate continues. A comparison of the calculated electron and hole states for a 28-Å InP QD using a 6-band  $\mathbf{k} \cdot \mathbf{p}$  model (76) and the direct diagonalization pseudopotential model (76) indicates that there are more electronic states for the latter than the former, and that in the latter the highest lying hole state is s-like rather than p-like. However, improvements in the  $\mathbf{k} \cdot \mathbf{p}$  parameters can reverse the character of the lowest level hole states and increase the total number of electronic states as well (74).

Because of the 3-D spatial confinement in QDs, the solution of the Schrödinger equation results in describing the electronic states in the QD by three quantum numbers plus spin. A commonly used notation (77, 78) is for the electron states to be labeled as  $nL_e$  and the hole states as  $nL_F$ , where  $n$  is the principal quantum number (1, 2, 3, etc),  $L$  is the orbital angular momentum (S, P, D, etc), and  $F$  is the total angular momentum ( $F = L + J$ , and  $J = L + S$ ), where  $S$  is the spin, and the projection of  $F$  along a magnetic axis is  $m_F = -F$  to  $+F$ . Thus, electron states become  $1S_e$ ,  $2S_e$ ,  $1P_e$ , etc, and hole states become  $1S_{1/2}$ ,  $1S_{3/2}$ , and  $1P_{1/2}$ , etc. For optical transitions in ideal spherical QDs, the selection rules are  $\Delta n = 0$ ,  $\Delta L = 0, \pm 2$ ; and  $\Delta F = 0, \pm 1$ . These ideal selection rules can be broken by nonspherical QDs and strong hole-state mixing.

## Synthesis of Quantum Dots

**Colloidal Quantum Dots** The most common approach to the synthesis of colloidal QDs is the controlled nucleation and growth of particles in a solution of chemical precursors containing the metal and the anion sources (controlled arrested precipitation) (79–81). The technique of forming monodisperse colloids is very old, and can be traced back to the synthesis of gold colloids by Michael Faraday in 1857 (80, 81). A common method for II-VI colloidal QD formation is to rapidly inject a solution of chemical reagents containing the group II and group VI species into a hot and vigorously stirred solvent containing molecules that can coordinate with the surface of the precipitated QD particles (79, 81, 82). Consequently, a large number of nucleation centers are initially formed, and the coordinating ligands in the hot solvent prevent or limit particle growth via Ostwald ripening (i.e. the growth of larger particles at the expense of smaller particles to minimize the higher surface free energy associated with smaller particles). Further improvement of the resulting size distribution of the QD particles can be achieved through size-selective precipitation (81, 82), whereby slow addition of a nonsolvent to the colloidal solution of particles causes precipitation of the larger-sized

particles (the solubility of molecules with the same type of chemical structure decreases with increasing size). This process can be repeated several times to narrow the size distribution of II-VI colloidal QDs to a few percent of the mean diameter.

The synthesis of colloidal III-V QDs is more difficult than for II-VI QDs because (a) the synthesis must be conducted in rigorously air-free and water-free atmospheres, (b) it generally requires higher reaction temperatures and much longer reaction times, and (c) it involves more complicated organometallic chemistry. The best results to date have been obtained for InP QDs (83–88). In this synthesis, an indium salt [ $\text{In}(\text{C}_2\text{O}_4)_3$ ,  $\text{InF}_3$ , or  $\text{InCl}_3$ ] is reacted with trimethylsilylphosphine [ $\text{P}(\text{Si}(\text{CH}_3)_3)_3$ ] in a solution of trioctylphosphine oxide (TOPO) and trioctylphosphine (TOP) to form a soluble InP organometallic precursor species that contains In and P in a 1:1 ratio. The InP precursor species in the TOPO/TOP solution is then heated for several days at a temperature ranging from 270 to 290°C, depending upon desired QD properties. A transmission electron microscope (TEM) picture of InP QDs showing lattice imaging is presented in Figure 8. One difference with the synthesis for II-VI materials is that more than 1 day of heating at reaction temperature is required to form crystalline III-V QDs, whereas II-VI QDs form immediately upon injection of the reactants into the hot TOPO/TOP solution.

The resulting InP QDs contain a capping layer of TOPO, which can be readily exchanged for several other types of capping agents, such as thiols, pyridines, amines, and polymers. The size distribution of the InP QDs can be further narrowed to less than 10% through selective precipitation techniques. Finally, they can be studied in the form of colloidal solutions or powders or dispersed in transparent polymers or organic (for low temperature studies) glasses; capped InP QDs recovered as powders can also be redissolved to form transparent colloidal solutions.

In addition to InP QDs, similar methods have been used to produce QDs of GaP (83, 89),  $\text{GaInP}_2$  (83, 89), GaAs (83, 89–92), and InAs (93); higher temperatures (400°C) are required for GaP and  $\text{GaInP}_2$  QDs. However, the quality (especially narrow size distributions) of these other III-V QDs is not yet as high as that obtained for InP QDs; this is primarily because less effort has been spent thus far on these other QD preparations.

**Quantum Dots Produced by Stranski-Krastinow Epitaxial Growth** QDs can also be produced via epitaxial growth from the vapor phase on appropriate substrates; the growth can be done using either MBE (see “*Molecular Beam Epitaxy*”) or MOCVD (see “*Metallo-Organic Chemical Vapor Deposition*”) systems. In the Stranski-Krastinow (SK) mode of QD formation, a thin semiconductor film is deposited by MBE or MOCVD onto another semiconductor substrate material that has a mismatch in lattice constant with the material being deposited. If the lattice mismatch is sufficiently high and the film has a higher surface energy than the substrate, then after the initial growth of a few monolayers (called the wetting layer), subsequent deposition forms small islands that are in the QD size regime. The size, shape, perfection, and density of these SK QDs can be controlled by controlling the conditions in the MBE or MOCVD reactor. The bulk of work on these SK QDs

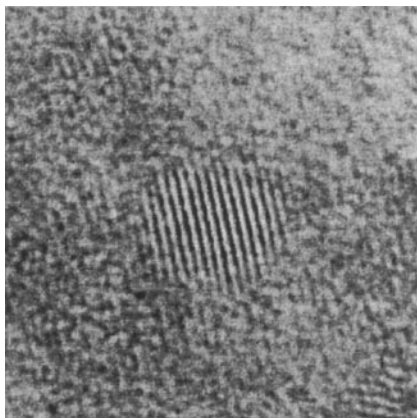
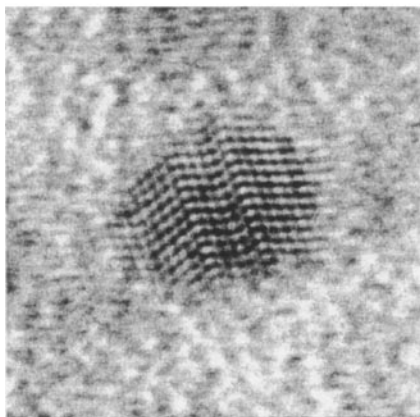


**Figure 8** High-resolution TEM of a 60-Å diameter InP QD oriented with the +111, axis in the plane of the micrograph. The bottom plate shows a rare dislocation defect.



has been on  $\text{InGa}_x\text{As}_{1-x}$  QDs grown on GaAs substrates (94); InP QDs grown on GaAs or  $\text{Al}_x\text{Ga}_{1-x}\text{As}$  substrates has also been reported (95), as has work on GeQDs on Si (95a). The size of SK QDs is generally larger than that of colloidal QDs; they typically have a lateral dimension of about 1000 to 2000 Å and a height of 100 to 500 Å. For III-V semiconductors these sizes produce quantization effects because their Bohr radius is large, but the degree of quantization is not as strong as that in colloidal QDs in which the sizes range from 15 to 100 Å. The shape of the InAs/GaAs SK QDs has been reported to be a square-based pyramid (96); however, recent results suggest a parallelogram base and  $C_{2v}$  symmetry (97, 98).

Another configuration of SK-type QDs is possible. In this case a quantum well (QW) is first formed that has a thin outer barrier (about 100 Å). SK islands of another semiconductor material having a lattice mismatch with the barrier are then deposited on top of the barrier. These SK islands produce a parabolic strain field that propagates down through the barrier into the QW. In the case of InP SK islands (called stressor islands) formed on an AlGaAs/GaAs/AlGaAs QW, the strain field expands the GaAs lattice and reduces the GaAs band gap in the QW just below the InP islands (95). Thus, the GaAs QW beneath the InP stressor islands is converted into a QD because the 1-D confinement of carriers is transformed into 3-D confinement. An important feature of this type of QD is that both the well and barrier region of the QD are made of the same material. This eliminates interface defects and interface states that complicate the relaxation behavior of photogenerated carriers.

## Optical Properties of Quantum Dots

In this section the optical properties of InP QDs are discussed. The optical properties of other III-V and II-VI QDs exhibit the same general behavior as InP QDs, and the latter is used to exemplify some of the important features of this behavior.

**Optical Absorption and Global Photoluminescence** The absorption and emission spectra of initially prepared InP QDs with a mean diameter of 32 Å are shown in Figure 1 of Reference 87. Optical absorption and PL spectra were collected at room temperature; samples were prepared by dispersing washed QDs in toluene.

The absorption spectrum shows an excitonic peak at about 590 nm. The PL spectrum (excitation at 500 nm) shows two emission bands: a weaker one near the band edge with a peak at 655 nm, and a second, stronger, broader band that peaks above 850 nm. The PL band with deep red-shifted subgap emission peaking above 850 nm is attributed to radiative recombination in QD surface states produced by phosphorous vacancies (87). These surface defects and the accompanying red-shifted emission can be completely removed by etching the InP QDs with hydrogen fluoride (HF); intense band-edge emission from the InP QDs can then be observed. After etching, the PL intensity increases by a factor of 10, and the near-infrared emission produced by the deep surface traps is completely removed (87). The near-band-edge quantum yield increases from 30% to 60% as the temperature decreases from 300 to 10 K (87).

The room temperature absorption spectra as a function of QD size ranging from 26 to 60 Å (measured by TEM) are shown in Figure 9 (88). The absorption spectra show one or more broad excitonic peaks that reflect substantial inhomogeneous line broadening arising from the QD size distribution; as expected, the spectra shift to higher energy as the QD size decreases (88). The color of the InP QD samples changes from deep red (1.7 eV) to green (2.4 eV) as the diameter decreases from 60 to 26 Å. Bulk InP is black with a room-temperature band gap of 1.35 eV and an absorption onset at 918 nm. Higher energy transitions above the first excitonic

peak in the absorption spectra can also be easily seen in QD samples with mean diameters equal to or greater than 30 Å. The spread in QD diameters is generally about 10% and is somewhat narrower in samples with larger mean diameters; this is why higher energy transitions can be resolved for the larger-sized QD ensembles. All the prepared QD nanocrystallites are in the strong confinement regime because the Bohr radius of bulk InP is about 100 Å. Figure 9 shows typical room-temperature absorption and global emission spectra of the InP colloids, with mean particle diameters ranging from 26 to 60 Å as measured by TEM (88); the excitation energy for all QD sample ensembles in Figure 9 was 2.48 eV, well above their absorption onset in each case.

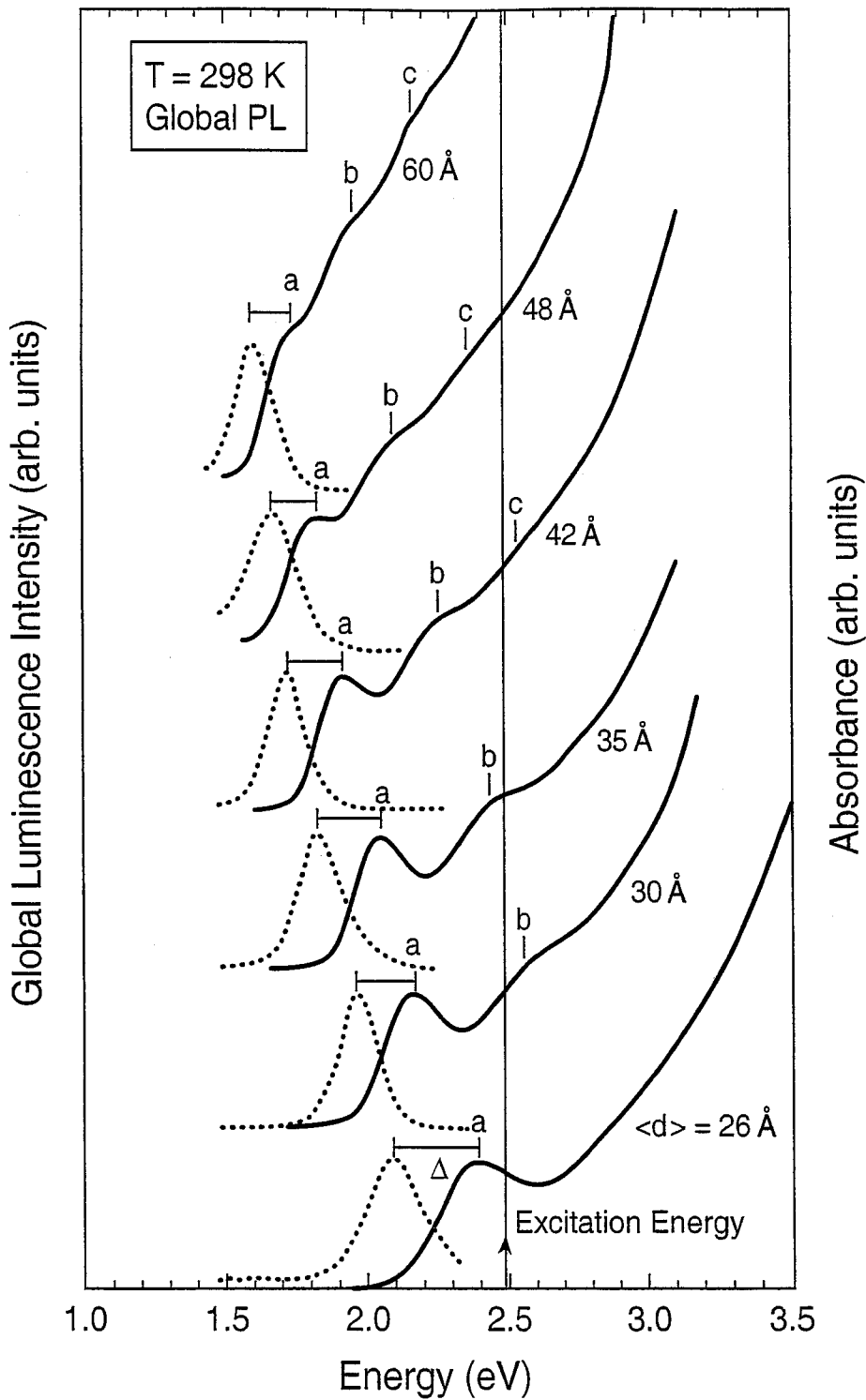
The global emission peaks in Figure 9 show an increasing red shift from the first excitonic absorption peak as the mean QD size decreases from 60 to 26 Å. The global (nonresonant) red shift is as large as 300 meV for samples with the smallest mean diameter (88). Global PL is defined as that observed when the excitation energy is much higher than the energy of the absorption threshold exhibited in the absorption spectrum produced by the ensemble of QDs in the sample; thus, a large fraction of all the QDs in the sample are excited. The resulting global PL shows a very broad peak (line width of 175–225 meV) that is red-shifted by 100–300 meV from the first absorption peak. The broad PL line width is caused by inhomogeneous line broadening arising from the ~10% size distribution sampled in the global PL experiment. The large global red shift is caused by the volume dominance of the larger particles in the size distribution; the latter will absorb most of the incident photons and will show large red shifts because the PL excitation energy is well above their lowest transition energy.

**Size-Selected Photoluminescence** If the excitation energy is restricted to the onset region of the absorption spectrum of the QD ensemble, then a much narrower range of QD sizes is excited; these QDs will have the larger particle sizes in the ensemble. Consequently, the PL spectra from this type of excitation show narrower line widths and smaller red shifts with respect to the excitation energy. This technique is termed fluorescence line narrowing (FLN), the resulting PL spectra being considerably narrowed.

FLN spectra at 10 K are shown in Figure 3 in Reference 88 for InP QDs with a mean diameter of 32 Å (88). FLN/PL spectra are shown for a series of excitation energies (1.895 eV to 2.07 eV) spanning the absorption tail near the onset of absorption for this sample (88). The global PL spectrum produced when the excitation energy (2.41 eV) is deep into the high-energy region of the absorption spectrum is also shown.

FLN spectra can be combined with photoluminescence excitation spectra to determine the resonant red shift (88). The resultant resonant red shift at  $T = 11$  K as a function of PL excitation energy ranges from 4 to 10 meV.

**Origin of Resonant Red Shift** The origin of the resonant red shift in InP has been recently analyzed theoretically (99, 100). Four possible models were considered, and the experimental results were consistent with a model in which the emission



is from an intrinsic, spin-forbidden state, split from its singlet counterpart owing to screened electron-hole exchange [dark exciton model (101, 102)].

The line widths of FLN spectra are typically 15–30 meV; although these line widths are significantly narrower than the 175–225 meV line widths typically obtained from global (nonresonant) PL excitation, they are still much broader than line widths reported from PL measurements on single dots. For a variety of II-VI and III-V QDs, single-dot PL line widths have been reported to range from 40–1000  $\mu\text{eV}$  (103–108); the experimental PL line widths observed for single QDs are smaller than the line widths obtained in Reference 88 by a factor of about 2 to 50. The broader line widths in the FLN spectra are attributed to the significant QD size and shape distribution that still remains in the FLN experiment. Also, the absorption peak moves about 35 to 45 meV for every 1-Å change in QD diameter. Thus, the PL line width of 15–30 meV for FLN spectra reflects a QD-diameter variation of less than 1 Å! It is apparent that the PL line width is extremely sensitive to the spread in QD diameters, and that the determination of true line widths requires PL data obtained from single dots.

## Phonon Bottleneck and Slowed Hot-Electron Cooling in Quantum Dots

The first prediction of slowed cooling at low light intensities in quantized structures was made by Boudreaux et al (10). They anticipated that cooling of carriers would require multiphonon processes when the quantized levels are separated in energy by more than phonon energies. They analyzed the expected slowed cooling time for hot holes at the surface of highly doped n-type  $\text{TiO}_2$  semiconductors, in which quantized energy levels arise because of the narrow space-charge layer (i.e. depletion layer) produced by the high doping level. The carrier confinement in this case is produced by the band bending at the surface; for a doping level of  $1 \times 10^{19} \text{ cm}^{-3}$  the potential well can be approximated as a triangular well extending 200 Å from the semiconductor bulk to the surface and with a depth of 1 eV at the surface barrier. The multiphonon relaxation time was estimated from

$$\tau_c \sim \omega^{-1} \exp(\Delta E/kT), \quad 24.$$

where  $\tau_c$  is the hot-carrier cooling time,  $\omega$  is the phonon frequency, and  $\Delta E$  is the energy separation between quantized levels. For strongly quantized electron levels, with  $\Delta E > 0.2 \text{ eV}$ ,  $\tau_c$  could be  $> 100 \text{ ps}$  according to Equation 24.

However, carriers in the space charge layer at the surface of a heavily doped semiconductor are only confined in one dimension, as in a quantum film. This quantization regime leads to discrete energy states that have dispersion in k-space

**Figure 9** Absorption (solid line) and global photoluminescence (dotted line) spectra at 298 K for colloidal ensembles of InP quantum dots with different mean diameters. All quantum dots colloidal samples were photoexcited at 2.48 eV (88).

(109). This means the hot carriers can cool by undergoing interstate transitions that require only one emitted phonon followed by a cascade of single phonon intrastate transitions; the bottom of each quantum state is reached by intrastate relaxation before an interstate transition occurs. Thus, the simultaneous and slow multiphonon relaxation pathway can be bypassed by single phonon events, and the cooling rate increases correspondingly.

More complete theoretical models for slowed cooling in QDs have been proposed recently by Bockelmann and co-workers (19, 110) and Benisty and co-workers (18, 20). The proposed Benisty mechanism (18, 20) for slowed hot-carrier cooling and phonon bottleneck in QDs requires that cooling only occurs via longitudinal optical (LO) phonon emission. However, there are several other mechanisms by which hot electrons can cool in QDs. Most prominent among these is the Auger mechanism (111). Here, the excess energy of the electron is transferred via an Auger process to the hole, which then cools rapidly because of its larger effective mass and smaller energy-level spacing. Thus, an Auger mechanism for hot-electron cooling can break the phonon bottleneck (111). Other possible mechanisms for breaking the phonon bottleneck include electron-hole scattering (112), deep-level trapping (113), and acoustical-optical phonon interactions (114, 115).

## Experimental Determination of Relaxation/Cooling Dynamics and a Phonon Bottleneck in Quantum Dots

Over the past several years many investigations have been published that explore hot-electron cooling/relaxation dynamics in QDs and the issue of a phonon bottleneck in QDs. The results are controversial, and it is quite remarkable that there are so many reports that both support (116–130) and contradict (113, 131–144) the prediction of slowed hot-electron cooling in QDs and the existence of a phonon bottleneck. One element of confusion that is specific to the focus of this review is that although some of these publications report relatively long hot-electron relaxation times (tens of ps) compared with what is observed in bulk semiconductors, the results are reported as being not indicative of a phonon bottleneck because the relaxation times are not excessively long and PL is observed (145–147). (Theory predicts an infinite relaxation lifetime of excited carriers for the extreme, limiting condition of a phonon bottleneck; thus, the carrier lifetime would be determined by nonradiative processes and PL would be absent.) However, because the interest here is on the rate of relaxation/cooling compared to the rate of electron transfer, we consider that slowed relaxation/cooling of carriers has occurred in QDs if the relaxation/cooling times are greater than 10 ps (about an order of magnitude greater than for bulk semiconductors). This is because previous work that measured the time of electron transfer from bulk III-V semiconductors to redox molecules (metallocenium cations) adsorbed on the surface found that electron transfer times can be sub-ps to several ps (28, 148–150); hence photoinduced hot electron transfer can be competitive with electron cooling and relaxation if the latter is greater than tens of ps.

In a series of papers Sugawara and colleagues (118, 119, 121) reported slow hot-electron cooling in self-assembled InGaAs QDs produced by Stranski-Krastinow (SK) growth on lattice-mismatched GaAs substrates. Using time-resolved PL measurements, the excitation-power dependence of PL, and the current dependence of electroluminescence spectra, these researchers reported cooling times ranging from 10 ps to 1 ns. The relaxation time increased with electron energy up to the fifth electronic state. Also, Mukai & Sugawara (151) recently published an extensive review of phonon bottleneck effects in QDs, which concludes that the phonon bottleneck effect is indeed present in QDs.

Gfroerer et al reported slowed cooling of up to 1 ns in strain-induced GaAs QDs formed by depositing tungsten stressor islands on a GaAs QW with AlGaAs barriers (130). A magnetic field was applied in these experiments to sharpen and further separate the PL peaks from the excited state transitions and thereby determine the dependence of the relaxation time on level separation. The authors observed hot PL from excited states in the QD, which could only be attributed to slow relaxation of excited (i.e. hot) electrons. Because the radiative recombination time is about 2 ns, the hot-electron relaxation time was found to be of the same order of magnitude (about 1 ns). With higher excitation intensity sufficient to produce more than one electron-hole pair per dot the relaxation rate increased.

A lifetime of 500 ps for excited electronic states in self-assembled InAs/GaAs QDs under conditions of high injection was reported by Yu et al (125). PL from a single GaAs/AlGaAs QD (128) showed intense high-energy PL transitions that were attributed to slowed electron relaxation in this QD system. Kamath et al (129) also reported slow electron cooling in InAs/GaAs QDs.

QDs produced by applying a magnetic field along the growth direction of a doped InAs/AlSb QW showed a reduction in the electron relaxation rate constant from  $10^{12} \text{ s}^{-1}$  to  $10^{10} \text{ s}^{-1}$  (120, 152).

In addition to slow electron cooling, slow hole cooling was reported by Adler et al (126, 127) in SK InAs/GaAs QDs. The hole relaxation time was determined to be 400 ps, based on PL rise times, whereas the electron relaxation time was estimated to be less than 50 ps. These QDs only contained one electron state but several hole states; this explained the faster electron cooling time because a quantized transition from a higher quantized electron state to the ground electron state was not present. Heitz et al (122) also report relaxation times for holes of about 40 ps for stacked layers of SK InAs QDs deposited on GaAs; the InAs QDs are overgrown with GaAs, and the QDs in each layer self-assemble into an ordered column. Carrier cooling in this system is about two orders of magnitude slower than in higher dimensional structures.

All of the above studies on slowed carrier cooling were conducted on self-assembled SK-type QDs. Studies of carrier cooling and relaxation have also been performed on II-VI CdSe colloidal QDs by Klimov et al (137, 153) and Guyot-Sionnest et al (116). The former group first studied electron relaxation dynamics from the first-excited 1P to the ground 1S state using interband pump-probe spectroscopy (137). The CdSe QDs were pumped with 100 fs pulses at 3.1 eV to create

high-energy electrons and holes in their respective band states, and then probed with fs white light continuum pulses. The dynamics of the interband bleaching and induced absorption caused by state filling was monitored to determine the electron relaxation time from the 1P to the 1S state. The results showed very fast 1P to 1S relaxation, on the order of 300 fs, and was attributed to an Auger process for electron relaxation that bypassed the phonon bottleneck. However, this experiment cannot separate the electron and hole dynamics from each other. Guyot-Sionnest et al (116) followed up these experiments using fs infrared pump-probe spectroscopy. A visible pump beam creates electrons and holes in the respective band states and a subsequent infrared beam is split into an infrared pump and an infrared probe beam; the infrared beams can be tuned to monitor only the intraband transitions of the electrons in the electron states and thus can separate electron dynamics from hole dynamics. The experiments were conducted with CdSe QDs that were coated with different capping molecules (TOPO, thiocresol, and pyridine), which exhibit different hole-trapping kinetics. The rate of hole trapping increased in the order: TOPO, thiocresol, and pyridine. The results generally show a fast relaxation component (1–2 ps) and a slow relaxation component ( $\approx 200$  ps). The relaxation times follow the hole-trapping ability of the different capping molecules and are longest for the QD systems having the fastest hole-trapping caps; the slow component dominates the data for the pyridine cap, which is attributed to its faster hole-trapping kinetics.

These results (116) support the Auger mechanism for electron relaxation, whereby the excess electron energy is rapidly transferred to the hole, which then relaxes rapidly through its dense spectrum of states. When the hole is rapidly removed and trapped at the QD surface the Auger mechanism for hot electron relaxation is inhibited and the relaxation time increases. Thus, in the above experiments, the slow 200 ps component is attributed to the phonon bottleneck, most prominent in pyridine-capped CdSe QDs, whereas the fast 1–2 ps component reflects the Auger relaxation process. The relative weight of these two processes in a given QD system depends upon the hole-trapping dynamics of the molecules surrounding the QD.

Klimov et al further studied carrier relaxation dynamics in CdSe QDs and published a series of papers on the results (153, 154); a review of this work was also recently published (155). These studies also strongly support the presence of the Auger mechanism for carrier relaxation in QDs. The experiments used ultrafast pump-probe spectroscopy with either two beams or three beams. In the former, the QDs were pumped with visible light across their band gaps (hole states to electron states) to produce excited state (i.e. hot) electrons; the electron relaxation was monitored by probing the bleaching dynamics of the resonant HOMO to LUMO transition with visible light or by probing the transient infrared absorption of the 1S to 1P intraband transition, which reflects the dynamics of electron occupancy in the LUMO state of the QD. The three-beam experiment was similar to that of Guyot-Sionnest et al (116) except that the probe in the experiments of Klimov et al is a white-light continuum. The first pump beam is at 3 eV and creates electrons and

holes across the QD band gap. The second beam is in the infrared and is delayed with respect to the optical pump; this beam repumps electrons that have relaxed to the LUMO back up in energy. Finally, the third beam is a broad-band white-light continuum probe that monitors photoinduced interband absorption changes over the range of 1.2 to 3 eV. The experiments were done with two different caps on the QDs: a ZnS cap and a pyridine cap. The results showed that with the ZnS-capped CdSe the relaxation time from the 1P to 1S state was about 250 fs, whereas for the pyridine-capped CdSe, the relaxation time increased to 3 ps. The increase in the latter experiment was attributed to a phonon bottleneck produced by rapid hole trapping by the pyridine, as also proposed by Guyot-Sionnest et al. However, the time scale of the phonon bottleneck induced by hole trapping by pyridine caps on CdSe that was reported by Klimov et al was not as great as that reported by Guyot-Sionnest et al.

In contradiction to the results discussed above, many other investigations exist in the literature in which a phonon bottleneck was apparently not observed. These results were reported for both self-organized SK QDs (113, 131–144) and II-VI colloidal QDs (137, 139, 141). However, in several cases (122, 145, 147), hot-electron relaxation was found to be slowed, but not sufficiently to enable the authors to conclude that this was evidence of a phonon bottleneck. For the issue of hot-electron transfer this conclusion may not be relevant because, in this case, one is not interested in the question of whether the electron relaxation is slowed so drastically that nonradiative recombination occurs and quenches photoluminescence, but rather whether the cooling is slowed sufficiently so that excited-state electron transport and transfer can occur across the semiconductor-molecule interface before cooling. For this purpose, the cooling time need only be increased above about 10 ps because electron transfer can occur within this time scale (28, 148–150).

The experimental techniques used to determine the relaxation dynamics in the above experiments showing no bottleneck were all based on time-resolved PL or transient absorption spectroscopy. The SK QD systems that were studied and that exhibited no apparent phonon bottleneck include  $\text{In}_x\text{Ga}_{1-x}\text{As}/\text{GaAs}$  and  $\text{GaAs}/\text{AlGaAs}$ . The colloidal QD systems were CdSs QDs in glass (750 fs relaxation time) (141) and CdSe (133). Thus, the same QD systems studied by different researchers showed both slowed cooling and nonslowed cooling in different experiments. This suggests a strong sample-history dependence for the results; perhaps the samples differed in their defect concentration and type, surface chemistry, and other physical parameters that affect carrier cooling dynamics. Much additional research is required to sort out these contradictory results.

## Quantum Dot Solar Cells

As mentioned above in the INTRODUCTION and “RELAXATION DYNAMICS OF HOT ELECTRONS IN QUANTUM DOTS,” slowed hot-carrier cooling in QDs can possibly be utilized to produce enhanced efficiencies for the conversion

of radiant energy into electrical or chemical potential energy. The two fundamental pathways for enhancing the conversion efficiency [increased photovoltage (9, 10) or increased photocurrent (11, 12)] can be accessed, in principle, in three different QD solar cell configurations. These are described below; however, it is emphasized that these potential high-efficiency configurations are speculative and that there is no experimental evidence yet that demonstrates actual enhanced conversion efficiencies in any of these systems.

***Photoelectrodes Composed of Quantum Dot Arrays*** In this configuration the QDs are formed into an ordered 3-D array with inter-QD spacing sufficiently small that strong electronic coupling occurs and minibands are formed to allow long-range electron transport. The system is a 3-D analog to the 1-D superlattice, and miniband structures discussed in “Energy Levels and Density of States in Quantum Wells and Superlattices” and shown in Figure 3. The delocalized quantized 3-D miniband states could be expected to slow the carrier cooling and permit the transport and collection of hot carriers to produce a higher photopotential in a photovoltaic cell or in a photoelectrochemical cell in which the 3-D QD array is the photoelectrode (156). Also, impact ionization might be expected to occur in the QD arrays, enhancing the photocurrent. However, hot-electron transport/collection and impact ionization cannot occur simultaneously; they are mutually exclusive, and only one of these processes can be present in a given system.

Significant progress has been made in forming 3-D arrays of both colloidal (157) and SK (94) II-VI and III-V QDs. The former have been formed via evaporation and crystallization of colloidal QD solutions containing a uniform QD size distribution; crystallization of QD solids from broader size distributions leads to close-packed QD solids, but with a high degree of disorder. Concerning the latter, arrays of SK QDs have been formed by successive epitaxial deposition of SK QD layers; after the first layer of SK QDs is formed, successive layers tend to form with the QDs in each layer aligned on top of each other (94, 158). Theoretical and experimental studies of the properties of QD arrays are currently under way. Major issues are the nature of the electronic states as a function of interdot distance, array order versus disorder, QD orientation and shape, surface states, surface structure/passivation, and surface chemistry. Transport properties of QD arrays are also of critical importance and are under investigation.

***Quantum Dot-Sensitized Nanocrystalline TiO<sub>2</sub> Solar Cells*** This configuration is a variation of a recent promising new type of photovoltaic cell that is based on dye sensitization of nanocrystalline TiO<sub>2</sub> layers (159–162). In this latter photovoltaic cell dye molecules are chemisorbed onto the surface of 10–30-nm TiO<sub>2</sub> particles that have been sintered into a highly porous nanocrystalline 10–20  $\mu\text{m}$  TiO<sub>2</sub> film. Upon photoexcitation of the dye molecules, electrons are very efficiently injected from the excited state of the dye into the conduction band of the

TiO<sub>2</sub>, affecting charge separation and producing a photovoltaic effect. The cell circuit is completed using a nonaqueous redox electrolyte that contains I<sup>-</sup>/I<sub>3</sub><sup>-</sup> and a Pt counter electrode to allow reduction of the adsorbed photooxidized dye back to its initial nonoxidized state (via I<sub>3</sub><sup>-</sup> produced at the Pt cathode by reduction of I<sup>-</sup>).

For the QD-sensitized cell QDs are substituted for the dye molecules; they can be adsorbed from a colloidal QD solution (163) or produced in situ (164–167). Successful photovoltaic effects in such cells have been reported for several semiconductor QDs including InP, CdSe, CdS, and PbS (163–167). Possible advantages of QDs over dye molecules are the tunability of optical properties with size and better heterojunction formation with solid hole conductors. Also a unique potential capability of the QD-sensitized solar cell is the production of quantum yields greater than one by the inverse Auger effect (impact ionization) (21). Dye molecules cannot undergo this process. Efficient inverse Auger effects in QD-sensitized solar cells could produce much higher conversion efficiencies than are possible with dye-sensitized solar cells

***Quantum Dots Dispersed in Organic Semiconductor Polymer Matrices*** Recently, photovoltaic effects have been reported in structures consisting of QDs forming junctions with organic semiconductor polymers. In one configuration, a disordered array of CdSe QDs is formed in a hole-conducting polymer—MEH-PPV [poly(2-methoxy, 5-(2'-ethyl)-hexyloxy-p-phenylenevinylene)] (168). Upon photoexcitation of the QDs, the photogenerated holes are injected into the MEH-PPV polymer phase and are collected via an electrical contact to the polymer phase. The electrons remain in the CdSe QDs and are collected through diffusion and percolation in the nanocrystalline phase to an electrical contact to the QD network. Initial results show relatively low conversion efficiencies (168, 169), but improvements have been reported with rod-like CdSe QD shapes (170) embedded in poly(3-hexylthiophene) (the rod-like shape enhances electron transport through the nanocrystalline QD phase). In another configuration (171), a polycrystalline TiO<sub>2</sub> layer is used as the electron-conducting phase, and MEH-PPV is used to conduct the holes; the electron and holes are injected into their respective transport mediums upon photoexcitation of the QDs.

A variation of these configurations is to disperse the QDs into a blend of electron- and hole-conducting polymers (172). This scheme is the inverse of light-emitting diode structures based on QDs (173–177). In the photovoltaic cell, each type of carrier-transporting polymer would have a selective electrical contact to remove the respective charge carriers. A critical factor for success is to prevent electron-hole recombination at the interfaces of the two polymer blends; prevention of electron-hole recombination is also critical for the other QD configurations mentioned above.

All of the possible QD–organic polymer photovoltaic cell configurations would benefit greatly if the QDs could be coaxed into producing multiple electron-hole pairs by the inverse Auger/impact ionization process (21). This is also true for

all the QD solar cell systems described in "Quantum Dot Solar Cells." The most important process in all the QD solar cells for reaching very high conversion efficiency is the multiple electron-hole pair production in the photoexcited QDs; the various cell configurations simply represent different modes of collecting and transporting the photogenerated carriers produced in the QDs.

## ACKNOWLEDGMENTS

I acknowledge and thank my present and former National Renewable Energy Laboratory (NREL) collaborators who have performed the NREL work reviewed here: OI Mičić, R Ellingson, M Hanna, BB Smith, DC Selmarten, Y Rosenwaks, K Jones, D Levi, MW Peterson, D Szmyd, and HM Cheong; I also thank A Zunger and H Fu for discussions on these topics. Finally, I am very grateful for the long-term and generous support of the US Department of Energy, Office of Science, Office of Basic Energy Sciences, Division of Chemical Sciences.

Visit the Annual Reviews home page at [www.AnnualReviews.org](http://www.AnnualReviews.org)

## LITERATURE CITED

1. Pankove JI. 1975. *Optical Processes in Semiconductors*. New York: Dover
2. Sze S. 1981. *Physics of Semiconductor Devices*. New York: Wiley
3. Stanton CJ, Bailey DW, Hess K, Chang YC. 1988. *Phys. Rev. B* 37:6575
4. Pelouch WS, Ellingson RJ, Powers PE, Tang CL, Szmyd DM, Nozik AJ. 1992. *Phys. Rev. B* 45:1450
5. Pelouch WS, Ellingson RJ, Powers PE, Tang CL, Szmyd DM, Nozik AJ. 1992. *Semicond. Sci. Technol.* B 7:337
6. Green MA. 1992. *Solar Cells*. Kensington, Aust.: Univ. New South Wales
7. Nozik AJ. 1978. *Annu. Rev. Phys. Chem.* 29:189
8. Sugawara M. ed. 1999. In *Semiconductors and Semimetals*. See Ref. 179, p. 86
9. Ross RT, Nozik AJ. 1982. *J. Appl. Phys.* 53:3813
10. Boudreaux DS, Williams F, Nozik AJ. 1980. *J. Appl. Phys.* 51:2158
11. Landsberg PT, Nussbaumer H, Willeke G. 1993. *J. Appl. Phys.* 74:1451
12. Kolodinski S, Werner JH, Wittchen T, Queisser HJ. 1993. *Appl. Phys. Lett.* 63:2405
13. Nozik AJ, Boudreaux DS, Chance RR, Williams F. 1980. In *Advances in Chemistry*, ed. M Wrighton, 184:162. New York: ACS
14. Williams FE, Nozik AJ. 1984. *Nature* 311:21
15. Nozik AJ. 1980. *Philos. Trans. R. Soc. London. Ser. A* 295:453
16. Rosenwaks Y, Hanna MC, Levi DH, Szmyd DM, Ahrenkiel RK, Nozik AJ. 1993. *Phys. Rev. B* 48:14675
17. Williams F, Nozik AJ. 1978. *Nature* 271:137
18. Benisty H, Sotomayor-Torres CM, Weisbuch C. 1991. *Phys. Rev. B* 44:10945
19. Bockelmann U, Bastard G. 1990. *Phys. Rev. B.* 42:8947
20. Benisty H. 1995. *Phys. Rev. B* 51:13281
21. Nozik AJ. 1997. Unpublished manuscript
22. Dingle R, Wiegmann W, Henry CH. 1974. *Phys. Rev. Lett.* 33:827
23. Weisbuch C, Vinter B. 1991. *Quantum*

- Semiconductor Structures*. New York: Academic
24. Bastard G. 1988. *Wave Mechanics Applied to Semiconductor Heterostructures*. New York: Halsted
  25. Jaros M. 1989. *Physics and Applications of Semiconductor Microstructures*. Oxford: Oxford Univ. Press
  26. Yoffe AD. 1993. *Adv. Phys.* 42:173
  27. Dingle R, ed. 1987. *Semiconductors and Semimetals*, Vol. 24. New York: Academic
  28. Miller RDJ, McLendon G, Nozik AJ, Schmickler W, Willig F. 1995. *Surface Electron Transfer Processes*. New York/Weinheim/Cambridge: VCH
  29. Peterson MW, Turner JA, Parsons CA, Nozik AJ, Arent DJ, et al. 1988. *Appl. Phys. Lett.* 53:2666
  30. Parsons CA, Thacker BR, Szymyd DM, Peterson MW, McMahon WE, Nozik AJ. 1990. *J. Chem. Phys.* 93:7706
  31. Bastard G. 1981. *Phys. Rev. B* 24:5693
  32. Bastard G. 1982. *Phys. Rev. B* 25:7594
  33. Altarelli M. 1985. *J. Lumin.* 30:472
  34. Bastard G, Brum JA. 1986. *J. Quantum Electron.* 22:1625
  35. Dingle R, Gossard AC, Wiegmann W. 1975. *Phys. Rev. Lett.* 34:1327
  36. Jung H, Fisher A, Ploog K. 1984. *Appl. Phys.* A33:97
  37. Reynolds DC, Bajaj KK, Litton CW. 1985. *Appl. Phys. Lett.* 46:51
  38. Aspnes DE. 1980. *Handbook on Semiconductors*. New York: North Holland
  39. Edelstein DC, Tang CL, Nozik AJ. 1987. *Appl. Phys. Lett.* 51:48
  40. Xu ZY, Tang CL. 1984. *Appl. Phys. Lett.* 44:692
  41. Rosker MJ, Wise FW, Tang CL. 1986. *Appl. Phys. Lett.* 49:1726
  42. Ryan JF, Taylor RA, Tuberfield AJ, Maciel A, Worlock JM, et al. 1984. *Phys. Rev. Lett.* 53:1841
  43. Christen J, Bimberg D. 1990. *Phys. Rev. B* 42:7213
  44. Cai W, Marchetti MC, Lax M. 1986. *Phys. Rev. B* 34:8573
  45. Nozik AJ, Parsons CA, Dunlavy DJ, Keyes BM, Ahrenkiel RK. 1990. *Solid State Commun.* 75:297
  46. Lugli P, Goodnick SM. 1987. *Phys. Rev. Lett.* 59:716
  47. Campos VB, Das Sarma S, Stroschio MA. 1992. *Phys. Rev. B* 46:3849
  48. Joshi RP, Ferry DK. 1989. *Phys. Rev. B* 39:1180
  49. Nirmal M, Dabbousi BO, Bawendi MG, Macklin JJ, Trautman JK, et al. 1996. *Nature* 383:802
  50. Efros AL, Rosen M. 1997. *Phys. Rev. Lett.* 78:1110
  51. Brus LE. 1984. *J. Chem. Phys.* 80:4403
  52. Brus LE. 1986. *J. Chem. Phys.* 90:2555
  53. Schmidt HM, Weller H. 1986. *Chem. Phys. Lett.* 129:615
  54. Ekimov AI, Efros AL, Ivanov MG, Onushenko AA, Shumilov SK. 1989. *Solid State Commun.* 69:565
  55. Kagan CR, Murray CB, Nirmal M, Bawendi MG. 1996. *Phys. Rev. Lett.* 76:1517
  56. Kayanuma Y, Momiji H. 1990. *Phys. Rev. B* 41:10261
  57. Kayanuma Y. 1988. *Phys. Rev. B* 38:9797
  58. Takagahara T. 1993. *Phys. Rev. B* 47:4569
  59. Takagahara T. 1993. *Phys. Rev. Lett.* 71:3577
  60. Hu YZ, Lindberg M, Koch SW. 1990. *Phys. Rev. B* 42:1713
  61. Park SH, Morgan RA, Hu YZ, Lindberg M, Koch SW, Peyghambarian N. 1990. *J. Opt. Soc. Am.* 7:2097
  62. Pollock EL, Koch SW. 1991. *J. Chem. Phys.* 94:6766
  63. Nomura S, Kobayashi T. 1991. *Solid State Commun.* 78:677
  64. Sercel PC, Vahala KJ. 1990. *Phys. Rev. B* 42:3690
  65. Efros AL. 1992. *Phys. Rev. B.* 46:7448
  66. Ekimov AI, Hache F, Schanne-Klein MC, Ricard D, Flytzanis C, et al. 1993. *J. Opt. Soc. Am. B* 10:100
  67. Grigoryan B, Kazaryan EM, Efros AL,

- Yazeva TV. 1990. *Sov. Phys. Solid State* 32:1031
68. Koch SW, Hu YZ, Fluegel B, Peyghambarian N. 1992. *J. Cryst. Growth* 117:592
69. Banyai L, Gilliot P, Hu YZ, Koch SW. 1992. *Phys. Rev. B* 45:14136
70. Banin U, Lee JC, Guzelian AA, Kadavanich AV, Alivisatos AP, et al. 1998. *J. Chem. Phys.* 109:2306
71. Fu H, Wang L-W, Zunger A. 1997. *Appl. Phys. Lett.* 71:3433
72. Fu H, Wang L-W, Zunger A. 1998. *Phys. Rev. B* 57:9971
73. Fu H, Wang L-W, Zunger A. 1998. *Appl. Phys. Lett.* 73:1157
74. Efros AL, Rosen M. 1998. *Appl. Phys. Lett.* 73:1155
75. Efros AL, Rosen M. 2000. *Annu. Rev. Mat. Sci.* 30:475
76. Fu H, Zunger A. 1998. *Phys. Rev. B* 57:R15064
77. Woggon U. 1997. *Optical Properties of Semiconductor Quantum Dots*. Berlin/Heidelberg: Springer-Verlag
78. Xia J-B. 1989. *Phys. Rev. B* 40:8500
79. Weller H, Eychmüller A. 1997. In *Semiconductor Nanoclusters—Physical, Chemical and Catalytic Aspects*. ed. PV Kamat, D Meisel, 103:5. Amsterdam: Elsevier
80. Overbeek JTG. 1982. *Adv. Colloid Interface Sci.* 15:251
81. Murray CB. 1995. *Synthesis and characterization of ii-vi quantum dots and their assembly into 3D quantum dot superlattices*. PhD thesis. MIT. Cambridge, MA
82. Murray CB, Norris DJ, Bawendi MG. 1993. *J. Am. Chem. Soc.* 115:8706
83. Mičić OI, Sprague JR, Curtis CJ, Jones KM, Machol JL, Nozik AJ. 1995. *J. Phys. Chem.* 99:7754
84. Banin U, Cerullo G, Guzelian AA, Bardeen CJ, Alivisatos AP, Shank CV. 1997. *Phys. Rev. B* 55:7059
85. Guzelian AA, Katari JEB, Kadavanich AV, Banin U, Hamad K, et al. 1996. *J. Phys. Chem.* 100:7212
86. Mičić OI, Curtis CJ, Jones KM, Sprague JR, Nozik AJ. 1994. *J. Phys. Chem.* 98:4966
87. Mičić OI, Sprague JR, Lu Z, Nozik AJ. 1996. *Appl. Phys. Lett.* 68:3150
88. Mičić OI, Cheong HM, Fu H, Zunger A, Sprague JR, et al. 1997. *J. Phys. Chem. B* 101:4904
89. Mičić OI, Nozik AJ. 1996. *J. Lumin.* 70:95
90. Olshavsky MA, Goldstein AN, Alivisatos AP. 1990. *J. Am. Chem. Soc.* 112:9438
91. Uchida H, Curtis CJ, Kamat PV, Jones KM, Nozik AJ. 1992. *J. Phys. Chem.* 96:1156
92. Nozik AJ, Uchida H, Kamat PV, Curtis C. 1993. *Isr. J. Chem.* 33:15
93. Guzelian AA, Banin U, Kadavanich AV, Peng X, Alivisatos AP. 1996. *Appl. Phys. Lett.* 69:1432
94. Sugawara M, ed. 1999. See Ref. 179, pp. 1–350
95. Hanna MC, Lu ZH, Cahill AF, Heben MJ, Nozik AJ. 1997. *J. Cryst. Growth.* 174:605
- 95a. Bimberg D, Grundmann M, Ledentsov NN. 1999. *Quantum Dot Heterostructures*, pp. 82–83. Chichester: Wiley
96. Ruminov S, Scheerschmidt K. 1995. *Phys. Status Solidi A* 150:471
97. Yang W, Lee H, Johnson TJ, Sercel PC, Norman AG. 2000. *Phys. Rev. B* 61:2784
98. Lee H, Yang W, Lowe-Webb R, Sercel PC. 1998. See Ref. 178, p. 205
99. Fu H, Zunger A. 1997. *Phys. Rev. B* 55:1642
100. Fu H, Zunger A. 1997. *Phys. Rev. B* 56:1496
101. Nirmal M, Norris DJ, Kuno M, Bawendi MG, Efros AL, Rosen M. 1995. *Phys. Rev. Lett.* 75:3728
102. Efros AL, Rosen M, Kuno M, Nirmal M, Norris DJ, Bawendi M. 1996. *Phys. Rev. B* 54:4843
103. Empedocles SA, Norris DJ, Bawendi MG. 1996. *Phys. Rev. Lett.* 77:3873

104. Forchel A, Steffen R, Koch T, Michel M, Albrecht M, Reinecke TL. 1996. *Semicond. Sci. Technol.* 11:1529
105. Gammon D, Snow ES, Katzer DS. 1995. *Appl. Phys. Lett.* 67:2391
106. Grundmann M, Christen J, Ledentsov NN, Bohrer J, Bimberg D, et al. 1995. *Phys. Rev. Lett.* 74:4043
107. Samuelson L, Carlsson N, Castrillo P, Gustafsson A, Hessman D, et al. 1995. *Jpn. J. Appl. Phys.* 34:4392
108. Nagamune Y, Watabe H, Nishioka M, Arakawa Y. 1995. *Appl. Phys. Lett.* 67:3257
109. Jaros M. 1989. In *Physics and Applications of Semiconductor Microstructures*, p. 83. New York: Oxford Univ. Press
110. Bockelmann U, Egeler T. 1992. *Phys. Rev. B* 46:15574
111. Efros AL, Kharchenko VA, Rosen M. 1995. *Solid State Commun.* 93:281
112. Vurgaftman I, Singh J. 1994. *Appl. Phys. Lett.* 64:232
113. Sercel PC. 1995. *Phys. Rev. B* 51:14532
114. Inoshita T, Sakaki H. 1992. *Phys. Rev. B* 46:7260
115. Inoshita T, Sakaki H. 1997. *Phys. Rev. B* 56:R4355
116. Guyot-Sionnest P, Shim M, Matranga C, Hines M. 1999. *Phys. Rev. B* 60: R2181
117. Wang PD, Sotomayor-Torres CM, McLelland H, Thoms S, Holland M, Stanley CR. 1994. *Surf. Sci.* 305:585
118. Mukai K, Sugawara M. 1998. *Jpn. J. Appl. Phys.* 37:5451
119. Mukai K, Ohtsuka N, Shoji H, Sugawara M. 1996. *Appl. Phys. Lett.* 68: 3013
120. Murdin BN, Hollingworth AR, Kamal-Saadi M, Kotitschke RT, Ciesla CM, et al. 1999. *Phys. Rev. B* 59:R7817
121. Sugawara M, Mukai K, Shoji H. 1997. *Appl. Phys. Lett.* 71:2791
122. Heitz R, Veit M, Ledentsov NN, Hoffmann A, Bimberg D, et al. 1997. *Phys. Rev. B* 56:10435
123. Heitz R, Kalburge A, Xie Q, Grundmann M, Chen P, et al. 1998. *Phys. Rev. B* 57:9050
124. Mukai K, Ohtsuka N, Shoji H, Sugawara M. 1996. *Phys. Rev. B* 54:R5243
125. Yu H, Lycett S, Roberts C, Murray R. 1996. *Appl. Phys. Lett.* 69:4087
126. Adler F, Geiger M, Bauknecht A, Scholz F, Schweizer H, et al. 1996. *J. Appl. Phys.* 80:4019
127. Adler F, Geiger M, Bauknecht A, Haase D, Ernst P, et al. 1998. *J. Appl. Phys.* 83:1631
128. Brunner K, Bockelmann U, Abstreiter G, Walther M, Böhm G, et al. 1992. *Phys. Rev. Lett.* 69:3216
129. Kamath K, Jiang H, Klotzkin D, Phillips J, Sosnowski T, et al. 1998. *Inst. Phys. Conf. Ser.* 156 (*Compound Semicond. Symp.* 1997):525
130. Gfroerer TH, Sturge MD, Kash K, Yater JA, Plaut AS, et al. 1996. *Phys. Rev. B* 53:16474
131. Li X-Q, Nakayama H, Arakawa Y. 1998. See Ref. 178, p. 845
132. Bellessa J, Voliotis V, Grousson R, Roditchev D, Gourdon C, et al. 1998. See Ref. 178, p. 763
133. Lowisch M, Rabe M, Kreller F, Henneberger F. 1999. *Appl. Phys. Lett.* 74:2489
134. Gontijo I, Buller GS, Massa JS, Walker AC, Zaitsev SV, et al. 1999. *Jpn. J. Appl. Phys.* 38:674
135. Li X-Q, Nakayama H, Arakawa Y. 1999. *Jpn. J. Appl. Phys.* 38:473
136. Kral K, Khas Z. 1998. *Phys. Status Solidi B* 208:R5
137. Klimov VI, McBranch DW. 1998. *Phys. Rev. Lett.* 80:4028
138. Bimberg D, Ledentsov NN, Grundmann M, Heitz R, Bohrer J, et al. 1997. *J. Lumin.* 72-74:34
139. Woggon U, Giessen H, Gindele F, Wind O, Fluegel B, Peyghambarian N. 1996. *Phys. Rev. B* 54:17681
140. Grundmann M, Heitz R, Ledentsov N,

- Stier O, Bimberg D, et al. 1996. *Superlattices Microstruct.* 19:81
141. Williams VS, Olbright GR, Fluegel BD, Koch SW, Peyghambarian N. 1988. *J. Mod. Opt.* 35:1979
142. Ohnesorge B, Albrecht M, Oshinowo J, Forchel A, Arakawa Y. 1996. *Phys. Rev. B* 54:11532
143. Wang G, Fafard S, Leonard D, Bowers JE, Merz JL, Petroff PM. 1994. *Appl. Phys. Lett.* 64:2815
144. Sandmann JHH, Grosse S, von Plessen G, Feldmann J, Hayes G, et al. 1997. *Phys. Status Solidi B* 204:251
145. Heitz R, Veit M, Kalburge A, Zie Q, Grundmann M, et al. 1998. *Physica E* 2:578
146. Li X-Q, Arakawa Y. 1998. *Phys. Rev. B* 57:12285
147. Sosnowski TS, Norris TB, Jiang H, Singh J, Kamath K, Bhattacharya P. 1998. *Phys. Rev. B* 57:R9423
148. Meier A, Selmarthen DC, Siemoneit K, Smith BB, Nozik AJ. 1999. *J. Phys. Chem. B* 103:2122
149. Meier A, Kocha SS, Hanna MC, Nozik AJ, Siemoneit K, et al. 1997. *J. Phys. Chem. B* 101:7038
150. Diol SJ, Poles E, Rosenwaks Y, Miller RJD. 1998. *J. Phys. Chem. B* 102:6193
151. Mukai K, Sugawara M. 1999. See Ref. 179, p. 209
152. Murdin BN, Hollingworth AR, Kamal-Saadi M, Kottischke RT, Ciesla CM, et al. 1998. See Ref. 178, p. 1867
153. Klimov VI, Mikhailovsky AA, McBranch DW, Leatherdale CA, Bawendi MG. 2000. *Phys. Rev. B* 61:R13349
154. Klimov VI, McBranch DW, Leatherdale CA, Bawendi MG. 1999. *Phys. Rev. B* 60:13740
155. Klimov VI. 2000. *J. Phys. Chem. B* 104:6112
156. Nozik AJ. 1996. Unpublished manuscript
157. Murray CB, Kagan CR, Bawendi MG. 2000. *Annu. Rev. Mater. Sci.* 30:611
158. Nakata Y, Sugiyama Y, Sugawara M. 1999. In *Semiconductors and Semimetals*, Vol. 60, ed. M Sugawara, 60:117. San Diego: Academic
159. Hagfeldt A, Grätzel M. 2000. *Acc. Chem. Res.* 33:269
160. Moser J, Bonnote P, Grätzel M. 1998. *Coord. Chem. Rev.* 171:245
161. Grätzel M. 2000. *Prog. Photovoltaics* 8:171
162. Kalyanasundaram K, Grätzel M. 1999. In *Optoelectronic Properties of Inorganic Compounds*, ed. DM Roundhill, JP Fackler Jr, p. 169. New York: Plenum
163. Zaban A, Mičić OI, Gregg BA, Nozik AJ. 1998. *Langmuir* 14:3153
164. Vogel R, Weller H. 1994. *J. Phys. Chem.* 98:3183
165. Weller H. 1991. *Ber. Bunsen-Ges. Phys. Chem.* 95:1361
166. Liu D, Kamat PV. 1993. *J. Phys. Chem.* 97:10769
167. Hoyer P, Könenkamp R. 1995. *Appl. Phys. Lett.* 66:349
168. Greenham NC, Peng X, Alivisatos AP. 1996. *Phys. Rev. B* 54:17628
169. Greenham NC, Peng X, Alivisatos AP. 1997. In *Future Generation Photovoltaic Technologies: First NREL Conference*, ed. R McConnell, p. 295. Am. Inst. Phys.
170. Huynh WU, Peng XG, Alivisatos AP. 1999. *Adv. Mater.* 11:923
171. Arango AC, Carter SA, Brock PJ. 1999. *Appl. Phys. Lett.* 74:1698
172. Nozik AJ, Rumbles G, Selmarthen DC. 2000. Unpublished manuscript
173. Dabbousi BO, Bawendi MG, Onitsuka O, Rubner MF. 1995. *Appl. Phys. Lett.* 66:1316
174. Colvin V, Schlamp M, Alivisatos AP. 1994. *Nature* 370:354
175. Schlamp MC, Peng X, Alivisatos AP. 1997. *J. Appl. Phys.* 82:5837
176. Mattoussi H, Radzilowski LH, Dabbousi

- BO, Fogg DE, Schrock RR, et al. 1999. *J. Appl. Phys.* 86:4390
177. Mattoussi H, Radzilowski LH, Dabousi BO, Thomas EL, Bawendi MG, Rubner MF. 1998. *J. Appl. Phys.* 83: 7965
178. Gershoni D, ed. 1998. *Proc. Int. Conf. Phys. Semicond. 24<sup>th</sup>* Singapore: World Sci.
179. Willardson RK, Weber ER, eds. 1999. *Semiconductors and Semimetals*, San Diego: Academic. Vol. 60



## CONTENTS

A Free Radical, <i>Alan Carrington</i>	1
State-to-State Chemical Reaction Dynamics in Polyatomic Systems: Case Studies, <i>James J Valentini</i>	15
Recent Progress in Infrared Absorption Techniques for Elementary Gas-Phase Reaction Kinetics, <i>Craig A Taatjes, John F Hershberger</i>	41
Surface Biology of DNA by Atomic Force Microscopy, <i>Helen G Hansma</i>	71
On the Characteristics of Migration of Oligomeric DNA in Polyacrylamide Gels and in Free Solution, <i>Udayan Mohanty, Larry McLaughlin</i>	93
Mechanisms and Kinetics of Self-Assembled Monolayer Formation, <i>Daniel K Schwartz</i>	107
Crossed-Beam Studies of Neutral Reactions: State-Specific Differential Cross Sections, <i>Kopin Liu</i>	139
Coincidence Spectroscopy, <i>Robert E Continetti</i>	165
Spectroscopy and Hot Electron Relaxation Dynamics in Semiconductor Quantum Wells and Quantum Dots, <i>Arthur J Nozik</i>	193
Ratiometric Single-Molecule Studies of Freely Diffusing Biomolecules, <i>Ashok A Deniz, Ted A Laurence, Maxime Dahan, Daniel S Chemla, Peter G Schultz, Shimon Weiss</i>	233
Time-Resolved Photoelectron Spectroscopy of Molecules and Clusters, <i>Daniel M Neumark</i>	255
Pulsed EPR Spectroscopy: Biological Applications, <i>Thomas Prisner, Martin Rohrer, Fraser MacMillan</i>	279
Fast Protein Dynamics Probed with Infrared Vibrational Echo Experiments, <i>Michael D Fayer</i>	315
Structure and Bonding of Molecules at Aqueous Surfaces, <i>GL Richmond</i>	357
Light Emitting Electrochemical Processes, <i>Neal R Armstrong, R Mark Wightman, Erin M Gross</i>	391
Reactions and Thermochemistry of Small Transition Metal Cluster Ions, <i>PB Armentrout</i>	423
Spin-1/2 and Beyond: A Perspective in Solid State NMR Spectroscopy, <i>Lucio Frydman</i>	463
From Folding Theories to Folding Proteins: A Review and Assessment of Simulation Studies of Protein Folding and Unfolding, <i>Joan-Emma Shea, Charles L Brooks III</i>	499
Polymer Adsorption-Driven Self-Assembly of Nanostructures, <i>Arup K Chakraborty, Aaron J Golubfskie</i>	537
Biomolecular Solid State NMR: Advances in Structural Methodology and Applications to Peptide and Protein Fibrils, <i>Robert Tycko</i>	575
Photofragment Translational Spectroscopy of Weakly Bound Complexes: Probing the Interfragment Correlated Final State Distributions, <i>L Oudejans, RE Miller</i>	607
Coherent Nonlinear Spectroscopy: From Femtosecond Dynamics to Control, <i>Marcos Dantus</i>	639
Electron Transmission through Molecules and Molecular Interfaces, <i>Abraham Nitzan</i>	681

Early Events in RNA Folding, <i>D Thirumalai, Namkyung Lee, Sarah A Woodson, DK Klimov</i>	751
Laser-Induced Population Transfer by Adiabatic Passage Techniques, <i>Nikolay V Vitanov, Thomas Halfmann, Bruce W Shore, Klaas Bergmann</i>	763
The Dynamics of "Stretched Molecules": Experimental Studies of Highly Vibrationally Excited Molecules with Stimulated Emission Pumping, <i>Michelle Silva, Rienk Jongma, Robert W Field, Alec M Wodtke</i>	811